Final Report for NNX13AR37G

SAMPLE RETURN SYSTEMS FOR EXTREME ENVIRONMENTS (SaRSEE)

R. M. Winglee, C. Truitt

Department of Earth and Space Sciences
University of Washington
Seattle WA 98195-1310

e-mail: winglee@ess.washington.edu

R. Hoyt

Tethers Unlimited Inc.
11711 N. Creek Pkwy S., Suite D113, Bothell WA 98011-8804

e-mail: hoyt@tethers.com

Table of Contents

1. **Abstract** 3
2. **The Importance of Sample Return Missions** 4
3. **Sample Return Methods** 5
4. **Penetrators and Space Exploration** 12
5. **SaSEE Mission Concept** 14
6. **Flight System Concepts** 17
7. **Penetrator Design** 19
8. **Field Testing** 27
    - **8.1 Phase I at Black Rock, Nevada, March 2013** 28
    - **8.2 Phase II at Naval Air Weapons Station, China Lake, June, 2014.** 32
    - **8.3 Phase II: 1st Field testing at Ione, CA, December, 2014** 33
    - **8.4 Phase II: 2nd Field testing at Ione, CA, March, 2015** 37
    - **8.5 Phase II: 3rd Field testing at Ione, CA, December, 2015** 44
9. **Recovery Systems –Tethers and Other Options** 46
    - **9.1 Tether Forces** 46
    - **9.2 Tether Spin-Up Maneuver** 48
10. **New Base-Line Concept** 49
11. **Modification of the Sample During High Velocity Impact** 53
12. **Conclusion** 57
13. **References** 58

14. Abstract

Sample return missions offer a greater science yield when compared to missions that only employ in situ experiments or remote sensing observations, since they allow the application of more complex technological and analytical methodologies in controlled terrestrial laboratories, that are both repeatable and can be independently verified. The successful return of extraterrestrial materials over the last four decades has contributed to our understanding of the solar system, but retrieval techniques have largely depended on the use of either soft-landing, or touch-and-go procedures that result in high ΔV requirements, larger spacecraft mass ratios, and return yields typically limited to a few grams of surface materials that have experienced varying degrees of alteration from space weathering. Hard-landing methods using planetary penetrators offer an alternative for sample return that significantly reduce a mission's ΔV and mass ratios, increase sample yields, and allow for the collection of subsurface materials, and lessons can be drawn from previous sample return missions. The following details progress in the design, development, and testing of penetrator/sampler technology capable of surviving subsonic and low, supersonic impact velocities (<700 m/s) that would enable the collection of geologic materials using tether technology to return the sample to a passing spacecraft. The testing of energy absorbing material for protecting the sample, design evolution and field testing of the penetrator, and dynamic modeling of tether behavior during sampling are discussed. It is shown through both modeling and field testing that penetrators at speeds between 300-600 m/s (~Mach 1-2) can penetrator into the ground to depths of 1-2 m with overall structural integrity attained. The first flight tests demonstrated the potential for survivability at these speeds. The second flight series demonstrated core sample collection with partial ejection of the sample return canister. The 3rd flight series demonstrated self-ejection of the sample return system fully intact and with the core retaining the full stratigraphy of the rock bed. The tether analysis shows that the forces on the tether during release and return of the sample to the main spacecraft are all at levels that can easily be handled by existing tether materials. The mass analysis of the requirements indicates that sample return form the asteroids could be handled with Discovery or New Frontier range of missions dependent on the number of samples to be returned to the Earth.

2. The Importance of Sample Return Missions

The National Research Council [2011] advised that Discovery and New Frontier class missions should play a critical role over the next decade in the study of primitive bodies given their relatively low cost and applicability for destinations both in the inner solar system, and beyond the asteroid belt. These missions will provide vital contributions in understanding the basic building blocks that created our world, as well as assessing potential hazards impacting bodies represent to our biosphere. Sample return missions from primitive bodies are excellent candidates for NASA's Discovery and New Frontier Programs given their potential for a high science yield while requiring only a fraction of the investment typical of a Flagship mission, and could supply materials long demanded by the science community for furthering our study of the solar system.

In the last decade, private industry's interest in reaching beyond Earth's gravitational influence has increased, as companies look to primitive bodies as a reservoir to augment limited terrestrial resources. The success of SpaceX's efforts in demonstrating civilian launch capabilities has encouraged investment in other organizations like Planetary Resources, and Deep Space Industries that intend to be among the first to harvest valuable metals from the asteroid belt. Table 1 shows a representative summary of important materials on extraterrestrial bodies that will play a critical role both in making these commercial ventures profitable, and in developing an understanding of the availability of supplies for In-Situ Resource Utilization (ISRU) for future space exploration [Mueller and Susante, 2012]. It is important to note the lack of confirmed data concerning asteroids and comets in the table, which represent gaps in our knowledge concerning their composition. Sample return missions from these bodies would help provide a map to the stars, increasing the efficiency of commercial exploration around the solar system, and assist in establishing the infrastructure necessary for humanity to push further into space by locating potential materials for ISRU.

Scott Sandford, a team member of the OSIRIS-REx mission speaking at an Exploration Science Forum, highlighted some of the advantages sample return missions have over in-situ and remote sensing methods, including: an increase in the quality of the data produced through the application of technology that was not available during the spacecraft's development; returned samples become research resources for both present and future scientists; sample analysis is not limited by design constraints of the spacecraft. He also spoke to their potential to reduce research limitations that result from poor assumptions saying, "…if you decide to measure *A*, and you go there with your *A* measuring machine… it is possible that the main thing that you will learn… is maybe you should have measured *B,* and now you need new spacecraft and another mission" [Sandford, 2014].The impact sample return missions will have on our understanding of the solar system cannot be understated, and given the high science yield, relatively low development cost, and long term benefits offered by analysis conducted in controlled terrestrial labs, these missions should have the highest priority in the years to come.

	Resources				
	Moon	**Mars**	**Asteroids**	**Comets**	**Outer Planets**
Regolith	H20 ice, O2, OH, Granular powder, Shielding, Insulation Structural, Manufacturing Feedstock	H20 ice, Rocky with sand, Shielding, Structural, Insulation, Manufacturing Feedstock	Varies – granular powder TBD	H20 ice TBD	TBD
Volatiles	H2O, CO, H2, Hg, H2S, NH3, He3, CH4, Ca, C2H6, CH3OH, C2H4	CO2, O, N2, H2O, Cl, Br, Fl, CO, TBD	H20, TBD	H20, CH4, TBD	H, He, CH4,N2 H2O, CO2, CO, NH4, C2H6 TBD
Minerals	Feldspars Pyroxines Olivines Oxides	Basalt Andecite Hematite Silicates Sulfates Carbonates Pegmatities Oxides, TBD	Silicates Oxides TBD	TBD	Silicates Oxides TBD
Metals	Al, Fe, Ti, Mg, Ca, TBD	Al, Fe, Ti, Mg, Ca, Na, Cu, Zn, Pb, Cr, Ni, Co, PGM, TBD	Fe, Ni, Ti, PGM et.c. TBD	TBD	Fe, TBD
Solar Power	Yes	Yes	Yes	Yes	No
Thermal gradients	Yes	Yes	Yes	Yes	Low
Vacuum	Yes	No: CO2, N2, H20, Ar, O2, CO, Ne, Kr, Xe, O3	Yes	Yes	No - varies
Rare Earth Elements	Yes associated with KREEP	TBD	TBD	TBD	TBD
Water	Limited - Poles	Yes	Yes	Yes	Yes - Abundant

Table 1. Representative known and unknown compositions of select extraterrestrial bodies, potential ISRU applications, and basic environmental considerations for visiting spacecraft; TBD = to be determined, PGM = platinum group metals, KREEP = potassium rare earth elements phosphorous [Mueller and Susante, 2012].

3. Sample Return Methods

The earliest evidence of the composition of other solid bodies arrived on Earth in the form of meteorites. Humans have been witness to meteorite falls and collecting their remnants for thousands of years, but only in more recent history has geochemistry began to unlock their compositional secrets. Stark differences in elemental ratios between the Earth and sampled meteorites, as well as between different meteorites themselves, have raised many questions

concerning the early formation of solid bodies. Figure 1 demonstrates differences in magnesium and aluminum abundances found in various terrestrial and extraterrestrial samples, along with compositional observations of the Sun's photosphere [Drake, 2002].

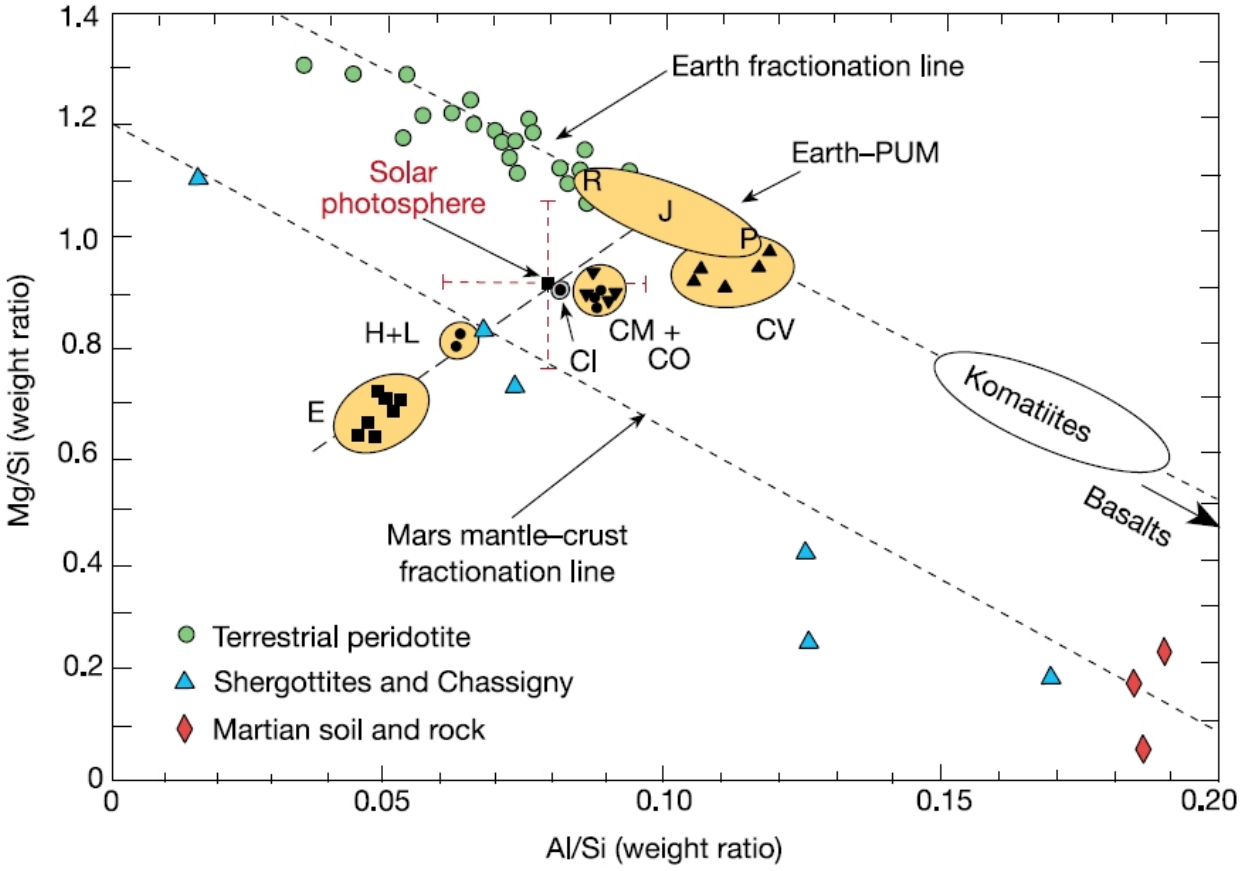

Figure 1. Mg/Si and Al/Si abundances of primitive material in the inner solar system; eclogite (E), ordinary (H, L) and carbonaceous (CI, CM, CO, CV) chondrites, primitive upper mantle (PUM) [Drake, 2002].

Primitive bodies in the solar system serve as reliquaries for the oldest materials that formed out of the solar nebula, but understanding their sources and the processes that created them requires a complexity of analysis that can only be achieved in controlled laboratory settings [Brucato et al, 2009]. The analysis of recovered meteorites has raised many questions concerning the asteroids that produced them. Over the last four decades, data concerning the composition of these bodies has been mainly limited to spectra and albedo observations either by orbiting telescopes like the Hubble Space Telescope, or by passing spacecraft like Galileo and Deep Space 1 [Shevchenko, 2005]. These direct observation methods have provided valuable information concerning the locations and general characteristics of many asteroids, but compositional information has been questioned due to various physical processes that are recognized to occur on the surface of asteroids. Shifts in the apparent spectra of rocky bodies can be caused both by impacts (shock darkening) and space weathering which red-shifts the

spectra of surface material [Chapman, 1996][Brunetto, 2009]. This alteration of surface materials was discovered during the earliest, and arguably most successful sample return missions during NASA's Apollo program.

If success is measured by the amount of sample material returned to Earth, the Apollo program, most noted for being the first exploration series to land humans on another rocky body, would be considered the most successful sample return missions to date. Between the summer of 1969 and winter of 1972, Apollo astronauts gathered and returned more than 300 kg of lunar material. While NASA employed human beings to collect material from the Moon, the Soviet's Luna program became the first automated system to return samples collected from a minor body, albeit in much smaller quantities. Figure 2 compares the return yields between the Apollo and Luna programs [Neal, 2009], and at first glance it seems obvious that manned sample return missions allow for the greatest collection of materials; however, manned missions are vastly more expensive, and current technology limits our ability to ensure the survivability of astronauts beyond low Earth orbit for extended periods of time.

Mission name	Location	Mass returned (kg)	Date returned
Apollo 11	Mare Tranquilitatis	21.6	24 July 1969
Apollo 12	Oceanus Procellarum	34.3	24 November 1969
Luna 16	Mare Fecunditatis	0.10	24 September 1970
Apollo 14	Fra Mauro (Mare Imbrium)	42.3	9 February 1971
Apollo 15	Hadley Rille/Appenine Mts	77.3	7 August 1971
Luna 20	Apollonius Highlands	0.03	25 February 1972
Apollo 16	Descartes Highlands	95.7	27 April 1972
Apollo 17	Taurus-Littrow/Mare Serenitatis	110.5	19 December 1972
Luna 24	Mare Crisium	0.17	22 August 1976

Figure 2. Lunar sample return yields for the Apollo and Luna programs [Neal, 2009].

The Apollo and Luna programs both employed soft-landing techniques, requiring the expenditure of considerable amounts of fuel to safely arrive on the Moon's surface, and additional propellant to ascend once collection efforts were completed. These maneuvers significantly increase a mission's ΔV budget, and require flawless execution to ensure the survival of sensitive instrumentation. Soft-landing on a minor body like a moon presents major technical challenges, but attempting the same Entry Descent and Landing (EDL) methods on a gravitationally negligible body is even more difficult as demonstrated by the recent Rosetta mission to Comet 67P/Churyumov-Gerasimenko (Figure 3)[Ulamec et al, 2014].

Having traversed more than six billion kilometers over the course of a decade, the Philae lander separated from its mothership, Rosetta, on November 12, 2014. In order to conduct its full suite of experiments on the comet's surface, Philae was designed to latch on to the comet through the use of a series of harpoons and ice screws. The failure of these systems to deploy resulted in the solar powered lander bouncing across the surface of the comet twice, coming to rest in an area it was incapable of recharging its batteries in, and after only 60 hours of operation the system went into hibernation and was not heard from again until sending an 85 second message back to Earth

on June 13, 2015 [Malik, 2015]. Despite the setbacks, the Rosetta mission has provided new information concerning the comet and although it was not a sample return mission, difficulties during its operation highlight the extreme challenges that soft-landing an automated spacecraft on a primitive body presents.

Figure 3. Artist's concept of the Philae lander after separating from the Rosetta spacecraft to begin a soft-landing EDL; Comet 67P/ Churyumov-Gerasimenko imaged by Rosetta's navigational camera [ESA, 2014].

To circumvent difficulties in keeping a lander on the surface of an asteroid, some sample return missions have utilized a touch-and-go approach. In these scenarios, sample retrieval is conducted as the spacecraft briefly contacts the surface of the sampling target, collecting a few grams of surface regolith before moving on. NASA's OSIRIS-REx spacecraft will employ this approach in 2019 to gather materials from asteroid 101955 Bennu by deploying its Touch-And-Go Sample Acquisition Mechanism (TAGSAM), shown in Figure 4. During contact with the surface, the TAGSAM will use a burst of nitrogen to blow regolith through a collecting sieve, and lab testing indicates that the method is capable of gathering more than 60 grams of material [NASA, nd]. The concept is not dissimilar to one attempted by JAXA's Hayabusa sampling of asteroid 25143 Itokawa in 2005, except that instead of using a nitrogen flushing system the spacecraft fired tantalum pellets at 300 m/s to collect the resulting ejecta inside its sampling mechanism [Yeomans, 2005]. Hayabusa demonstrated that touch-and-go sampling is possible, despite having crash-landed on Itokawa during a sampling attempt and collecting less than 1 mg

of material [Todd, 2015]; however, touch-and-go sampling limits collection to surface regolith and as such, Hayabusa2 (Figure 5) will deploy a kinetic impactor at the surface of asteroid 1999 JU3 in 2019, creating an artificial crater and collecting samples from greater depths than its predecessor [JAXA, 2003]. The touch-and-go method of sample return avoids the problems of attaching a spacecraft to an asteroid and helps to reduce a mission's ΔV budget, but still represents substantial risk to the spacecraft due to the close proximity the vehicle must get to the primitive body in order to complete sampling.

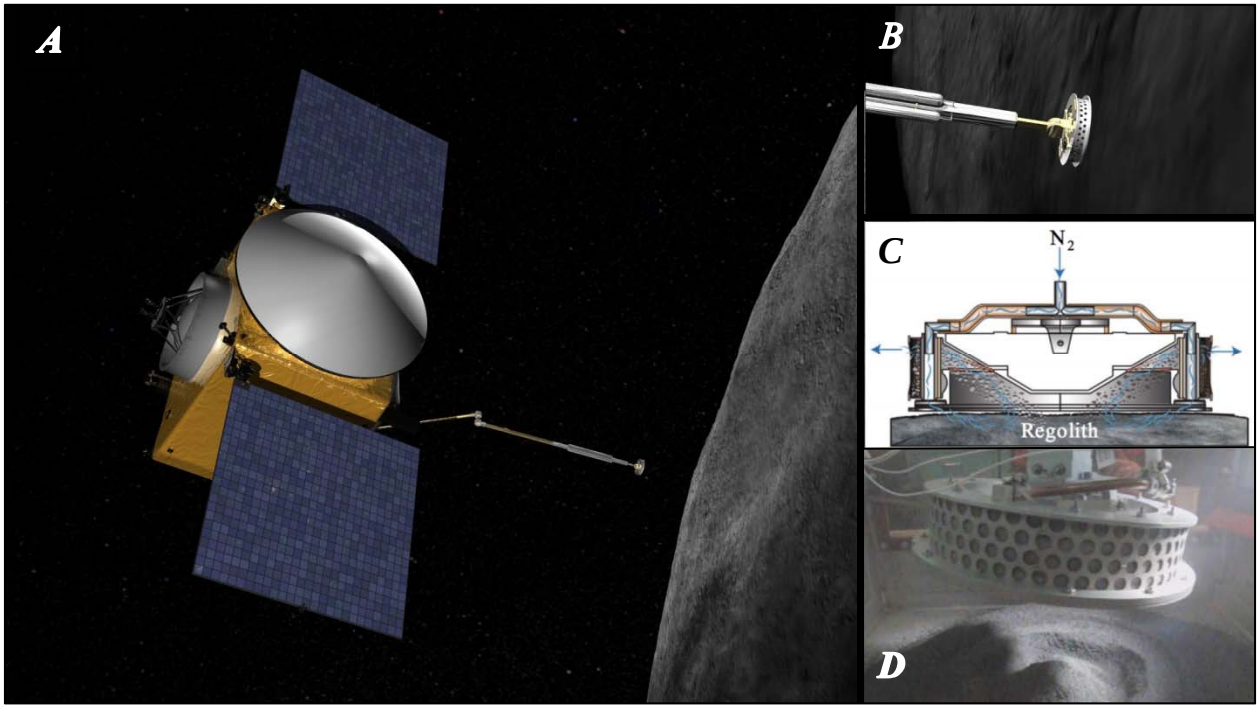

Figure 4. (A) Artist's concept of the OSIRIS-REx spacecraft deploying the TAGSAM instrument, (B) close-up of the TAGSAM head [Neal-Jones and Steigerwald, 2013]; (C) schematic showing the TAGSAM Nitrogen flush method of sample collection, (D) laboratory testing of the TAGSAM head [Marín, 2014].

Another method used in sample return missions avoids direct contact with the targeted body completely. NASA's first sample return efforts after Apollo 17 was the Genesis mission, (Figure 6) designed to characterize and sample the solar wind using a halo orbit around Lagrange point 1. The spacecraft gathered samples using collector arrays from late 2001 to spring of 2004, but the failure of its parachutes to deploy during Earth re-entry in September 2004 caused the Sample Return Capsule (SRC) to impact the landing zone at more than 86 m/s, resulting in the loss and contamination of significant amounts of sample material [Meyer, 2009]. In contrast, the Stardust spacecraft (Figure 7), sent to collect samples from Comet 81P/Wild 2, enjoyed a much better success.

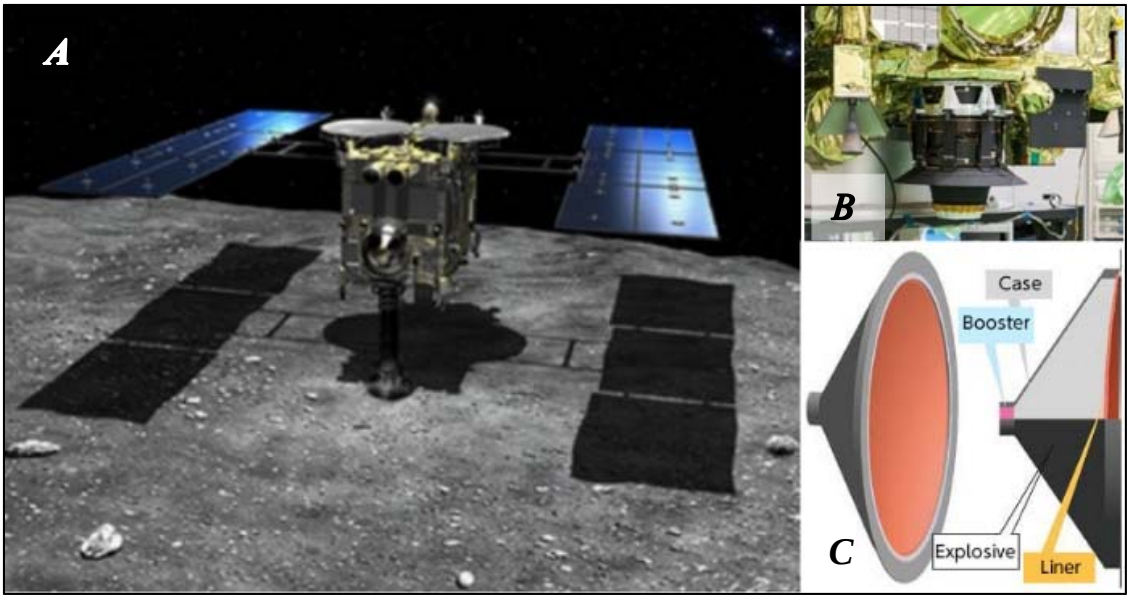

Figure 5. (A) Artist's concept of Hayabusa2 during touch-and-go sampling, showing its sampler mechanism (SMP) deployed and in contact with the asteroid, (B) the SMP onboard Hayabusa2 in its stowed configuration, (C) diagram showing the Small Carry-on Impactor (SCI) that will use explosives to reach an impact velocity of 2 km/s in order to facilitate the subsurface sampling of asteroid 1999 JU3 [JAXA, 2003].

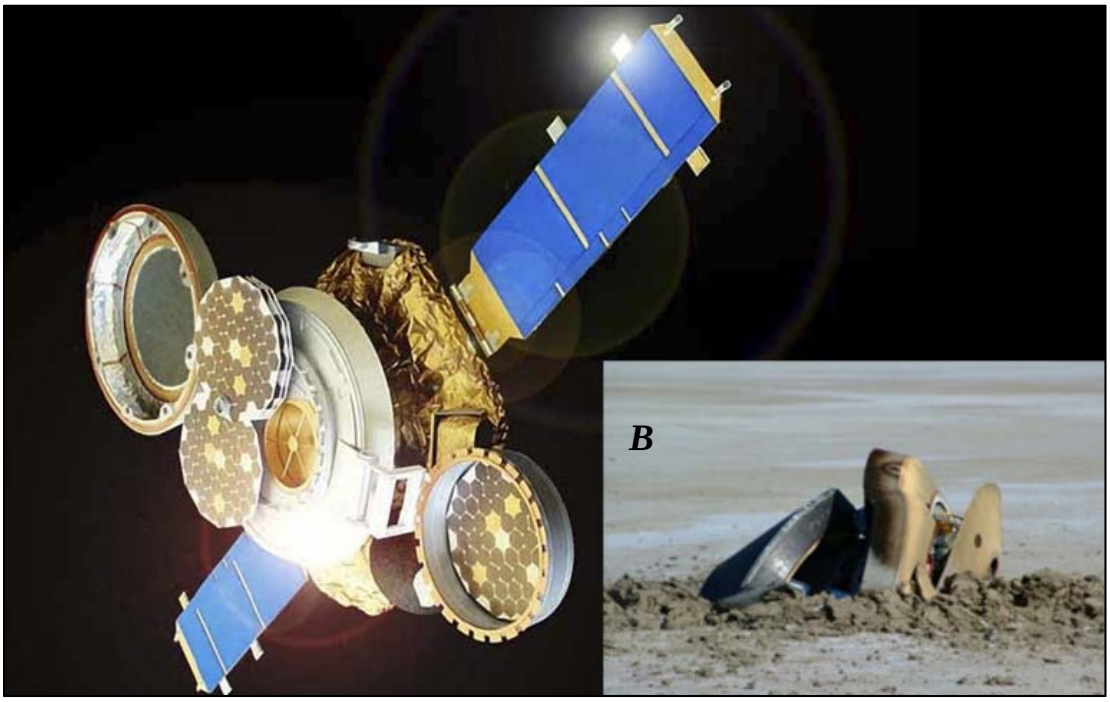

Figure 6. (A) Artist's concept of Genesis with its collection arrays deployed, (B) the impacted SRC [Meyer,2009].

Launched in early 1999, the Stardust mission first collected samples of interstellar dust in 2000, and again in 2002 following an Earth gravity assist trajectory. The mission's flight team performed a close flyby of asteroid 5535 Annefrank, using the opportunity as an engineering test of ground and spacecraft operations prior to intercepting Comet 81P/Wild 2 in 2004, where it flew through the halo of gases and dust at the head of the comet [Whalen, 2009]. The spacecraft used an Aerogel filled grid to collect materials thought to pre-date the birth of the Sun, and their successful return to Earth in 2006 has provided new insights into our solar system.

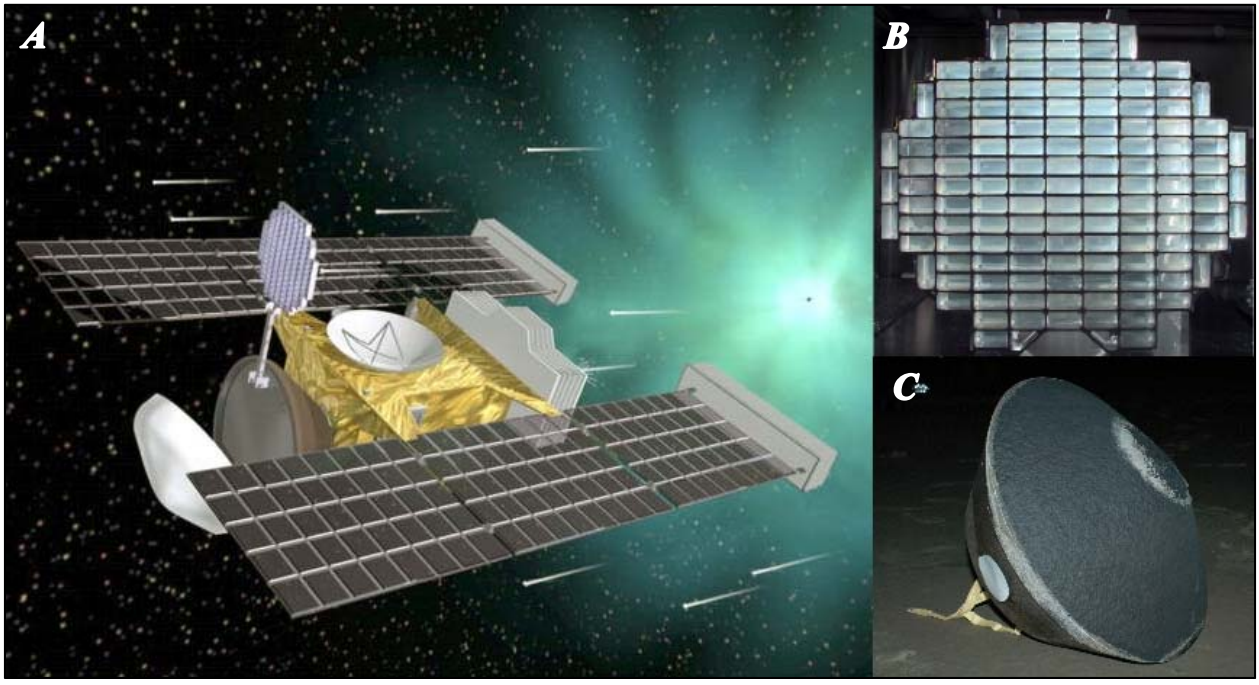

Figure 7. (A) Artist's concept of the Stardust spacecraft approaching Comet81P/ Wild 2 with its Collector Grid deployed, (B) the Aerogel filled Collector Grid prior to integration, (C) the SRC after successfully landing[Whalen, 2009].

The aforementioned missions highlight the difficulties associated with sample return missions. No-contact methods that protect the spacecraft are not easily applied to most primitive bodies and touch-and-go techniques limit collection to altered surface materials, while soft-landing missions require considerably more propellant mass and increases to a mission's ΔV budget. Penetrators deployed from a passing spacecraft could reduce a sample return mission's ΔV since no additional expenditure of propellant would be required for descent/ascent on a primitive body, and adequate distances between spacecraft and the impacted target would prevent impact ejecta from damaging the spacecraft, but to date no penetrators have been intended for sample return missions.

4. Penetrators and Space Exploration.

The lineage of planetary penetrators can be traced back to World War II and the development of ground penetrating munitions. The hardening of military fortifications was augmented by their construction at ever increasing depths below the surface, dictating advances in the weapons intended to destroy them. These early bunker-busters (Figure 8*A*) were large and heavy to provide effective penetration, requiring their deployment at high altitudes in order to maximize their impact velocity. Over the following decades the scale of these systems decreased allowing their application toward intelligence gathering as well, such as the USAF Igloo White Program (Figure 8*B*). These espionage penetrators demonstrated the ability for sensitive instrumentation to survive and operate after 2000 g impacts, and the systems were examples of the application of early data compressing technology designed to minimize communication and bandwidth requirements [Lorenz, 2011].

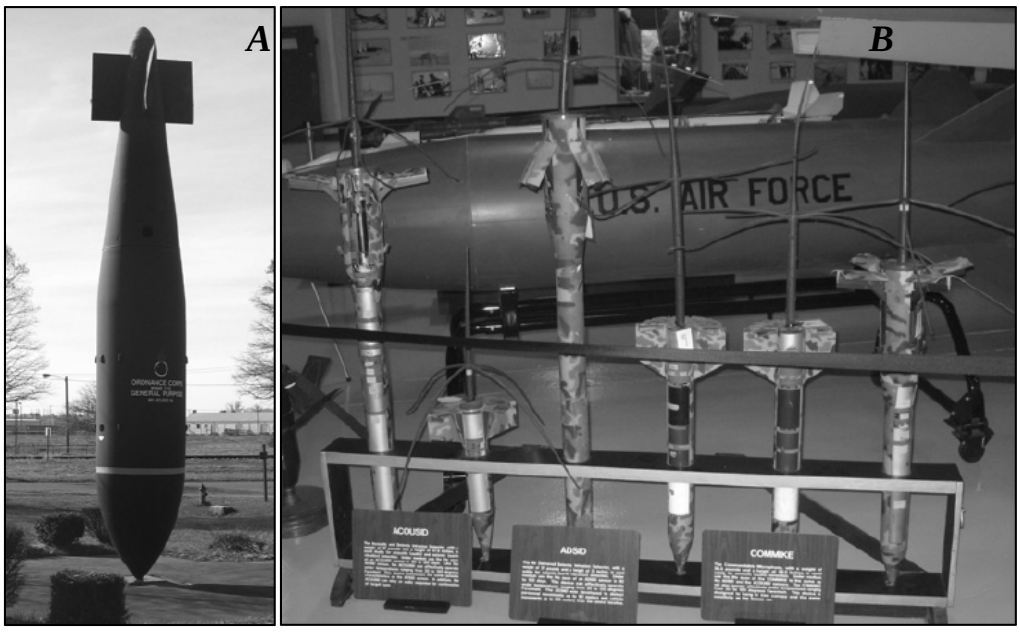

Figure 8. (A) The T-12 "Cloudmaker", (B) instrumented penetrators from the Igloo White Program [Lorenz, 2011].

The use of penetrators for space exploration was proposed as early as 1969 with suggestions that a Mars penetrator be used in conjunction with the Viking mission to search for subsurface water [Lorenz, 2011]. Over the following decades, multiple design proposals for embedding instrumentation during a Martian mission were brought forward given the limitations orbiting spacecraft and landers have in conducting surface observations. The Mars-96 penetrator, shown in Figure 9*A*, intended to deliver instrumentation for geophysical, meteorological, and compositional in situ analysis of the Martian environment [Surkov and Kremnev, 1998]. The Deep Space 2 (DS-2) mission probes (Figure 9B) were the first planetary penetrators sent to Mars, carried by the Mars Polar Lander (MPL); however, as the spacecraft

entered Mars' atmosphere, anomalies occurred during EDL and neither the MPL or DS-2 probes were ever heard from again [JPL Special Review Board, 2000].

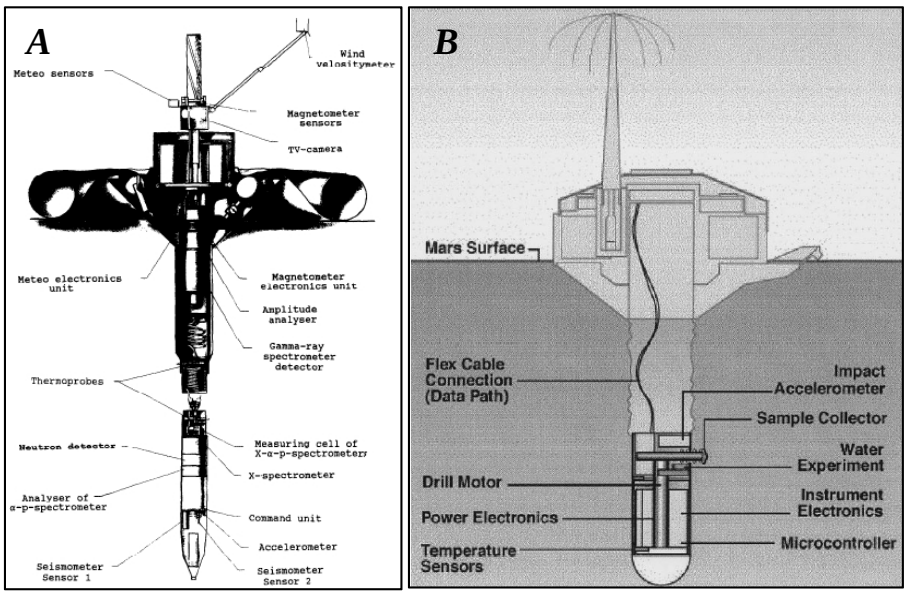

Figure 9. (A) Schematic for the Mars-96 penetrator [Surkov and Kremnev, 1998], (B) schematic for the DS-2 probe [Lorenz et al, 2000].

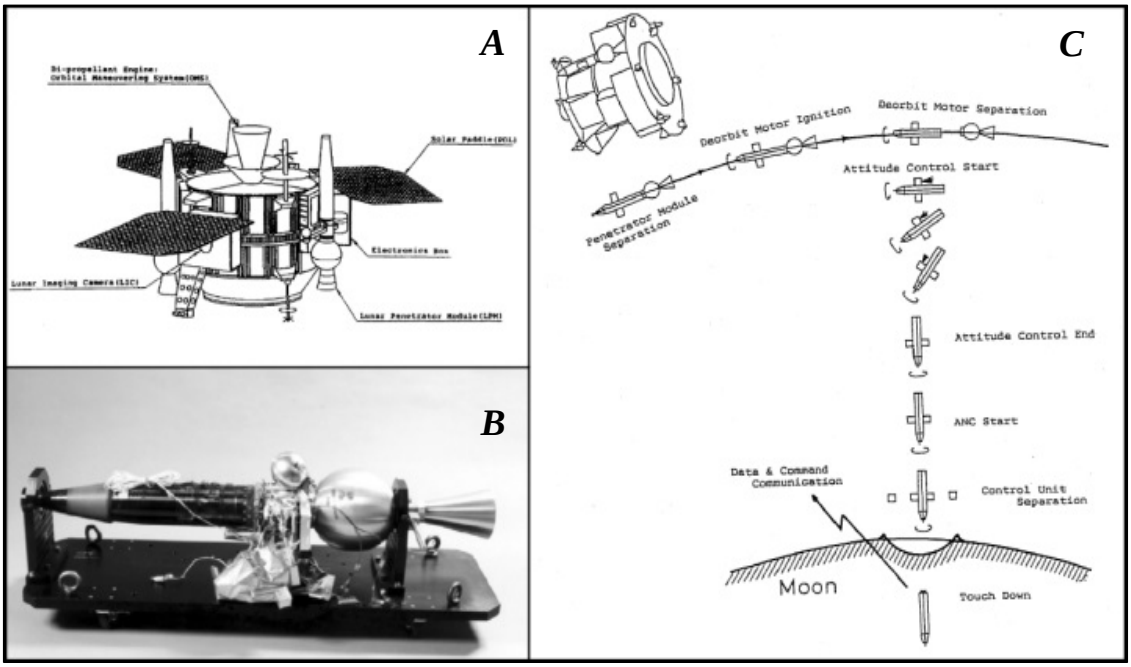

Figure 10. (A) Illustration of JAXA's LUNAR-A spacecraft [Nakajima et al, 1996], (B) a LUNAR-A LPM [Lorenz, 2011], (C) diagram depicting LUNAR-A penetrator deployment [Mizutani, 1995].

Embedding instrumentation in the surface of Mars is complicated by the planet's atmosphere, since aerodynamic affects need to be considered during EDL. Most minor bodies in

the solar system are devoid of any atmosphere, making the use of penetrators for scientific investigation easier. The LUNAR-A mission (Figure 10) intended to use three Lunar Penetrator Modules (LPMs) to further our understanding of the origin and evolution of the Moon. The LPMs, designed to impact around 275 m/s to a depth of about 2 meters, carried highly sensitive seismometers and heat probes to collect data that would be transmitted back to Earth via the orbiting spacecraft every 15 days [Mizutani, 1995]. The LPMs would separate from their orbiting mothership one at a time, and use solid state motors to achieve velocities low enough to deorbit and free fall to the lunar surface. The process was planned to take roughly one month to deploy all LPMs, embedding two on the near side and one on the far side of the Moon. Unfortunately, development of the LPMs took much longer than planned resulting in components populated in the mothership becoming obsolete, and the project was canceled in 2007 [ISAS, 2008].

5. SaRSEE Mission Concept

Over the centuries that humanity has observed the heavens, the major bodies (planets) have received the lion's share of attention, but their numbers represent only a small portion of the bodies that inhabit our solar system. To date we have identified more than 150,000 asteroids in the main belt alone [Asphaug, 2009], but difficulties in collecting samples has resulted in returning limited material from only one, asteroid 25143 Itokawa [Yano et al, 2006]. Figure 11 highlights the general location of many of the asteroids, as well as a representative comparison of escape/orbital velocities for select minor bodies that could serve as potential candidates for the SaRSEE mission concept. The following mission scenario takes advantage of these smaller velocities and avoids hazards experienced in earlier missions by protecting the main spacecraft by maintaining a safe distance from the targeted body. Additionally, the use of penetrators for

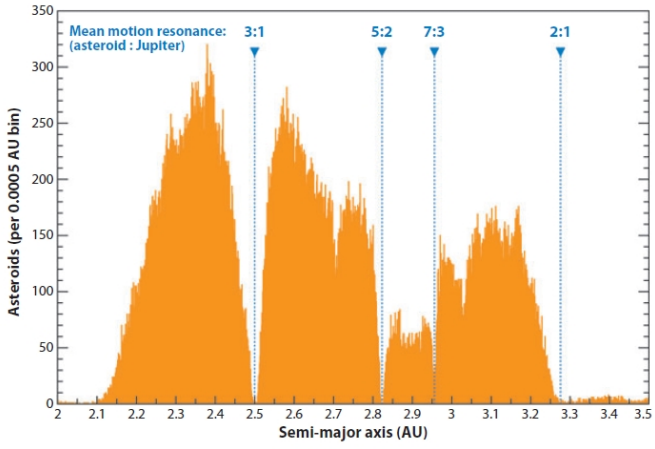

PLANETOID	MASS	RADIUS	V_{esc}	V_{orb}
	(10^{20} kg)	(km)	$(2GM/R)^{1/2}$	$(3GM/4R)^{1/2}$
208 Lacrimosa	0.00043	20.5	16.7	8.8
Chiron	0.04	90	77.0	45.3
Mimas	0.37	196.5	159.5	95.9
Enceladus	1.10	252	241.3	145.6
Pallas	2	272	321.7	194.3
1994VK8	4	389	370.4	224.6
Vesta	3	263	390.1	235.5
Tethys	6	531	394.7	240.0
Ceres	10	487	523.4	318.1
Dione	11	561	511.4	311.1
Iapetus	18	734	572.0	348.5
Charon	17	586	622.1	378.5
Rhea	23	763	634.1	386.4
Titania	35	789	769.3	468.9

Figure 11. A histogram showing radial distanct in AU of more than 150,000 asteroids [Asphaug, 2009], and a table of select minor bodies comparing escape and orbit velocities [Winglee et al, 2013].

sample collection allows for subsurface sampling of materials unaltered by space weathering, while tether technology used for retrieval reduces a mission's ΔV budget since no propellant expenditure is required for landing and ascending from the surface of a primitive body.

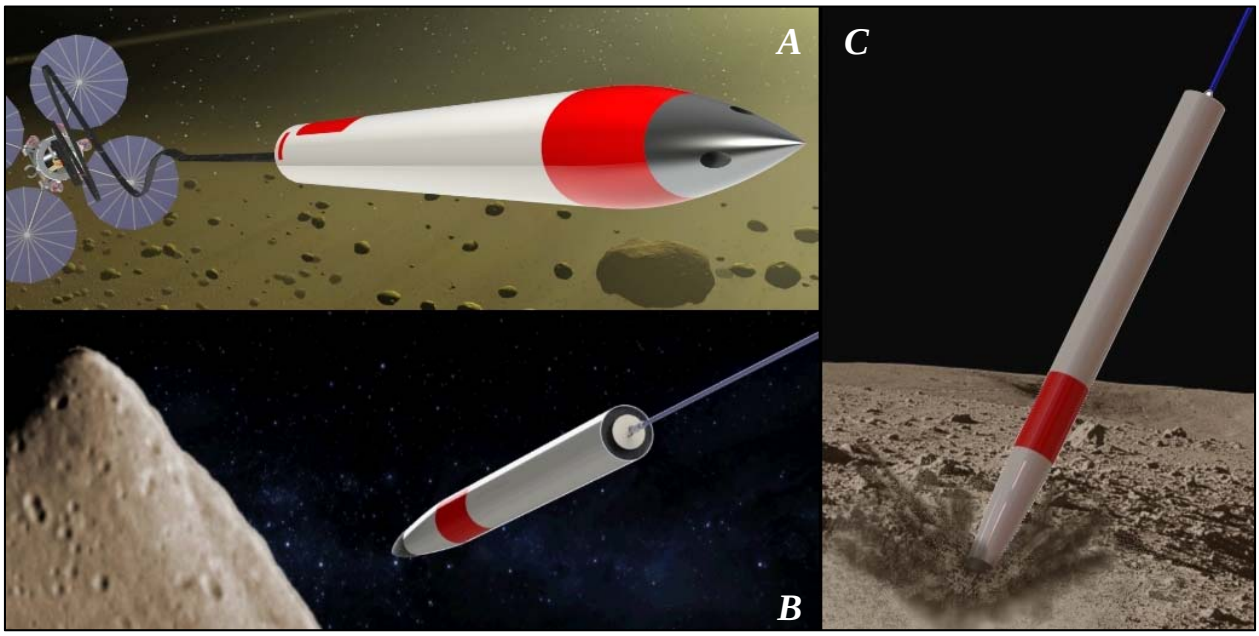

Figure 12. (A) Artist's concept of the spacecraft deploying a tethered penetrator,(B) followed by the descent to the target's surface, (C) and the resulting impact.

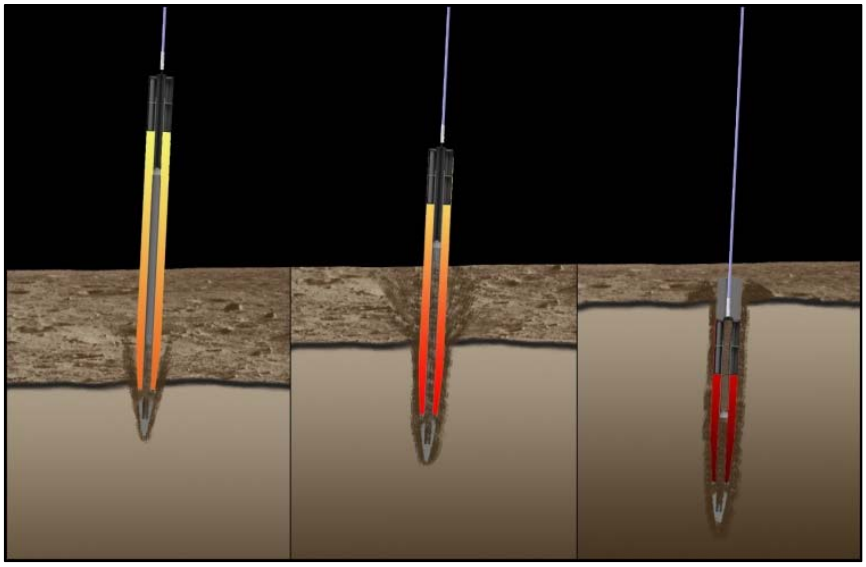

Figure 13. Artist's concept of sampling during the impact process. Material flows through the penetrator to a SRC at the aft of the penetrator.

In the SaRSEE mission concept, the spacecraft deploys a tethered penetrator as it approaches the sampling target, shown in Figure 12. The penetrator descends to the target surface, using the momentum imparted by the spacecraft to generate the necessary impact velocity (<700 m/s) to penetrate more than one meter below the surface. During the impact, feed ports in the nose cone allow material to flow up through the center

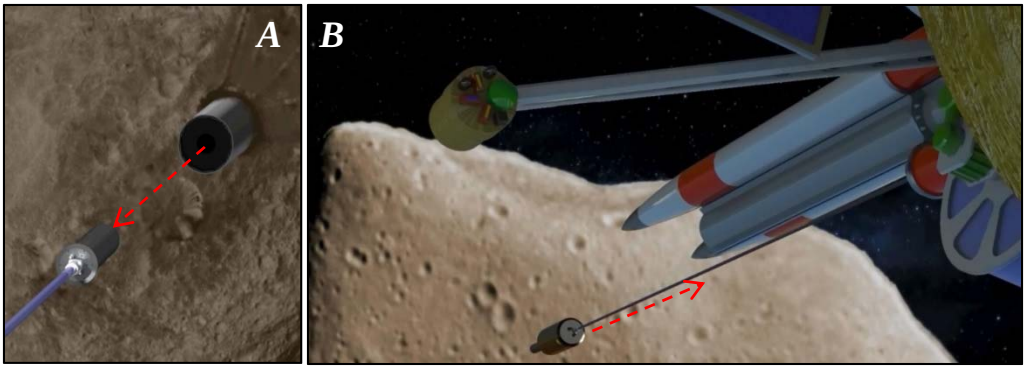

Figure 14. (A) Artist's concept showing the SRC extraction that leaves the rest of the penetrator in situ, (B) and its recovery to the spacecraft via the tether without requiring the spacecraft to land.

of the penetrator to the SRC at the aft of the penetrator (Figure 13). Energy absorbing material protects the SRC from the impacting forces while the main body of the penetrator is compressed along its length. The SRC, still tethered to the spacecraft, is ejected during collection by the flow of incoming sample material, and is reeled back to the mothership for containment; alternately, the SRC could be released by the spacecraft on a Earth return trajectory. By using the kinetic energy of the spacecraft, the SaRSEE concept reduces the mission's ΔV requirements, and as such offers better mass ratios that lower the expense of sample return missions and allow for subsurface sampling with estimated return yields of about 3-5 kg per impact. Comparisons between applied tether technology and chemical propulsion mass ratios are shown in Figure 15.

SaRSEE's reduced mass ratios open the potential to sample multiple targets of interest along a well-planned trajectory, or the ability to sample multiple locations on a single target depending on whether the spacecraft performs a fly-by of a primitive body (which may be ideal for smaller members of the population) or orbits the object. The same sampling concept could also be applied terrestrially, without the need for a spacecraft, for application in environments too hostile to risk sending a human being into. The ability to collect irradiated samples in the first few days following the containment failure at the Fukushima I Nuclear Power Plant in 2011 could have eliminated the need for volunteers to enter the hazard zone, for example. There has also been interest in using the technology for collecting samples from active volcanic eruptions that are too dangerous for scientists to enter.

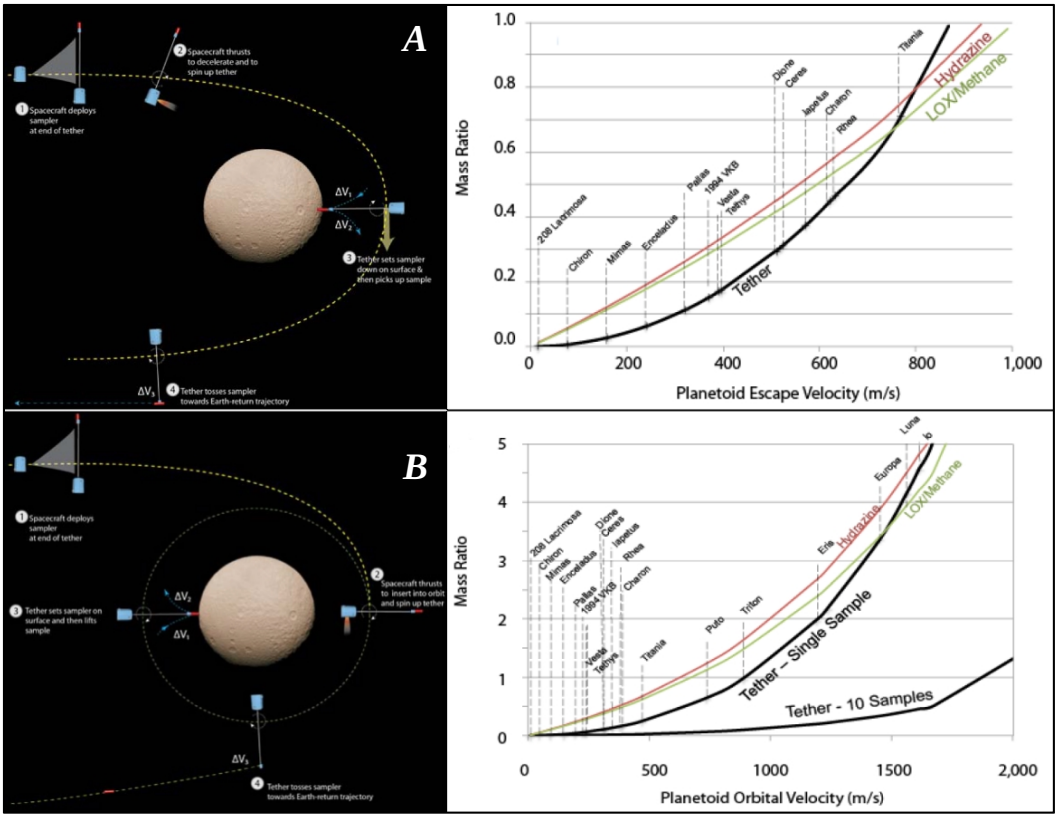

Figure 15. (A) Conceptual schematic for a fly-by SaRSEE mission with mass ratio comparison for 2XΔV; (B) mission concept for orbital sampling with mass ratio comparison showing multiple samples collected [Winglee et al, 2013].

6. Flight System Concepts

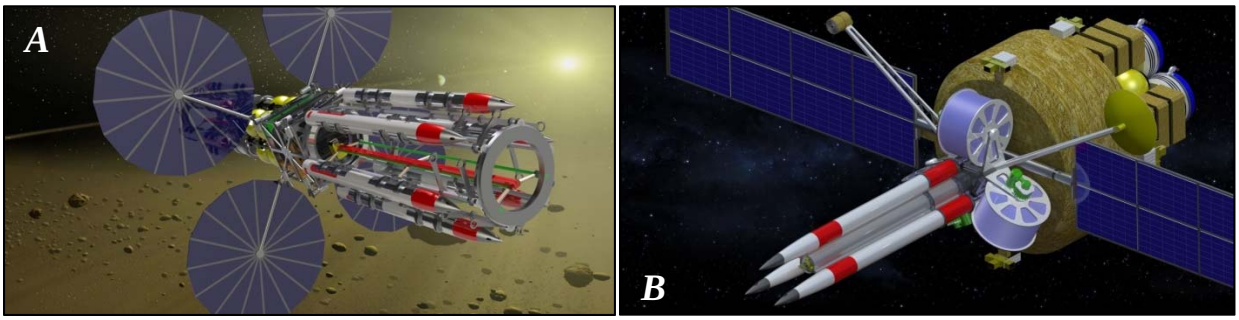

Figure 16. (A) A revolver-style flight system concept proposed during NIAC Phase I in which the spacecraft (~1500 kg) is equipped with at least six penetrators that share a single tether, (B) a shared-guide rail flight system concept proposed for NIAC Phase II showing the spacecraft (~1200 kg) equipped with three penetrators, each with an independent tether. Both systems rely on electric propulsion for cruise and attitude control, and are solar powered for traversing the inner solar system.

An additional advantage the use of penetrators for sample return missions offers is the variability in the spacecraft that could deploy them. Figure 16 shows configurations for two

early concepts: (*A*) a revolver-style loading system in which multiple penetrators can be cycled through, connecting to a single tether before deployment for the recovery of each SRC; (*B*) a single, shared-guide rail concept in which each penetrator is connected to an independent tether. Masses for each system were estimated from preliminary SolidWorks models, however it is important to note given limited resources and time lines involved in this Phase II study, these designs are conceptual at best and further development would be required to create a more accurate mass estimate, and possibly lead to lower mass estimates as systems as optimized for performance. The provided estimates do allow an initial cost estimate for development and construction of SaRSEE if the conceptual masses are compared to the expense and weight of previous sample return missions, shown in Figure 17.

Based on the initial conceptual mass for each system, development and construction of SaRSEE ranges between $550 to $775 million dollars, placing it above the current Discovery spending cap of $500 million and below the New Frontiers cap of $1 billion dollars [National Research Council, 2011]. It is easily conceivable that with adequate development, the mass of

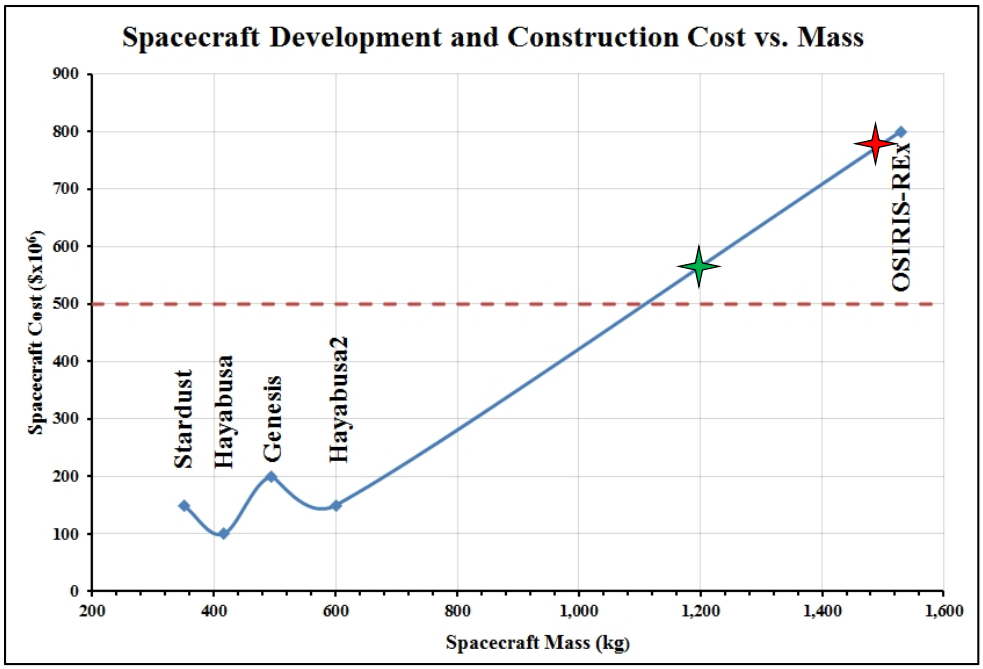

Figure 17. A comparison of the cost of development and construction for the last five sample return missions, and the masses of their respective spacecraft; the red-dashed line shows the current spending cap for Discovery class missions, while the cap for New Frontiers class missions is above the shown spending range. The green (16B) and red (16A) stars show the mass estimates for the flight systems shown in Figure 16.

the final SaRSEE spacecraft could fall within the Discovery class spending parameters, if the assumed relationship between cost and spacecraft mass is relatively correct. Additionally, the increase in sample yield (~3 kg per impact) significantly improves the return on investment since three of the plotted sample return missions in Figure 17 brought back less than 1 mg of material,

with results from Hayabusa2 and OSIRIS-REx pending. Alternately, the penetrators' mass could be reduced for a lower sample return yield, or fewer penetrators mounted on the spacecraft to allow the cost of the SaRSEE system to fall within Discovery class spending limits. Table 2 compares the sample return yield and mission development costs, showing the use of penetrators for sample return missions could greatly improve the return on their investment.

Mission	~ Cost ($x10^6)	~ Material Yield (kg)	Yield to Cost Ratio (kg/$x10^6)
Stardust	150	$1x10^{-6}$	$6.67x10^{-9}$
Hayabusa	100	$1x10^{-6}$	$1x10^{-8}$
Genesis	494	N/A (particles)	N/A
Hayabusa2	600	$1x10^{-2}$	$1.67x10^{-5}$
OSIRIS-REx	800	2	$2.5x10^{-3}$
SaRSEE	770	3 (per impact)	**>$3.9x10^{-3}$**

Table 2. Return yield to mission cost comparison, green missions complete, yellow missions pending.

7. Penetrator Design

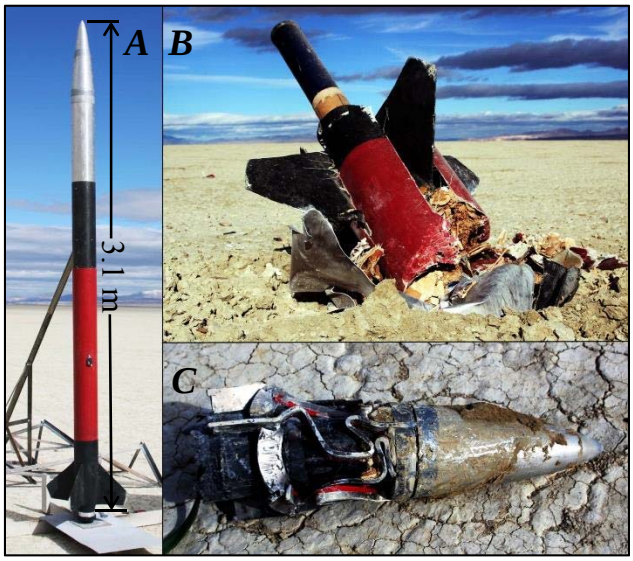

Figure 18. The Aluminum Rocket Prototype (ARP) inspired the design work that became the SaRSEE penetrator; (A) ARP pre-launch, (B) post-impact showing motor casing nearly ejected, (C recovered nose cone intact with deformed stringers that absorbed the impact energy.

Inspiration for the design of the SaRSEE penetrator originated during annual field testing at Black Rock, Nevada, in March of 2012 by students enrolled in the Rockets and Instrumentation course offered at the University of Washington's Department of Earth and Space Sciences. The Aluminum Rocket Prototype (Figure 18) was the first attempt at integrating aluminum structures into the composite materials normally used by the class, consisting of a solid aluminum nose cone, and internal aluminum rib-and-stringer skeleton. While the rocket launched as expected, a power anomaly at apogee prevented the recovery charges from firing, resulting in a ballistic impact. During recovery, it was observed the motor casing was nearly ejected intact, and the nose cone experienced no deformation. The rocket embedded to a depth of ~0.71 m, and while most of the airframe was destroyed, the rib-and-stringer infrastructure had absorbed much of the impact energy that resulted in minimal damage to the motor casing.

Figure 19 shows the basic internal layout for the SaRSEE penetrator, consisting of the machined nose cone equipped with feed ports, the crumple zone where energy absorbing layers

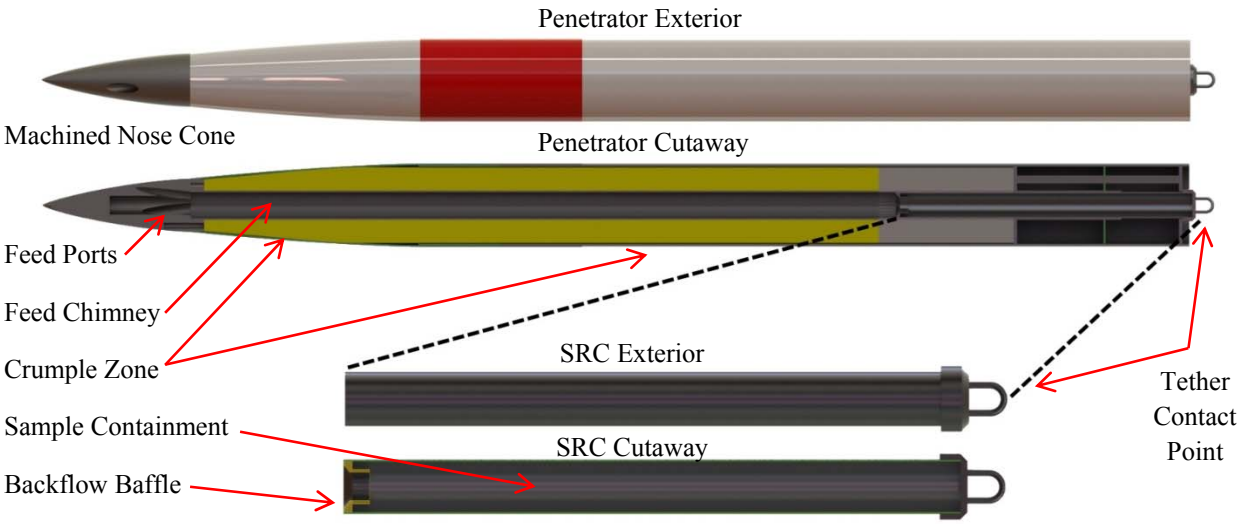

Figure 19. Simple schematic of the SaRSEE penetrator showing internal sections and the SRC.

of composite materials surround the feed chimney, and the SRC that also serves as the tether contact point. Ejecta flows through the feed ports and up the chimney, collecting in the SRC, so development of energy absorbing materials was critical to ensure the SRC would survive the impact.

Honeycombed aluminum structures have a long history of use in aerospace applications given their high strength-to-weight properties, and as such were optimal candidates for use as light weight, energy absorbing structures in the penetrator's crumple zone. Early estimates calculated the material would need to endure 500 kN of force before total failure to protect the SRC during impact, so test samples using Hexcel® aluminum honeycomb material were developed [Winglee et al, 2013]. Compression testing was conducted using an Instron 5585H Series Floor Model Testing System (Figure 20) capable of providing a maximum load of 250 kN for 75x75x16 mm test samples. When the honeycombed aluminum is compressed along the axis of the cells, the cell walls collapse in a concertina-like manner, and test samples were treated with various additives to fill the cell voids and increase the strength of the material (Figure 21). These additives were found to both

Figure 20. The Instron 5585H Series Floor Model Testing System used for compression testing [Winglee et al, 2013].

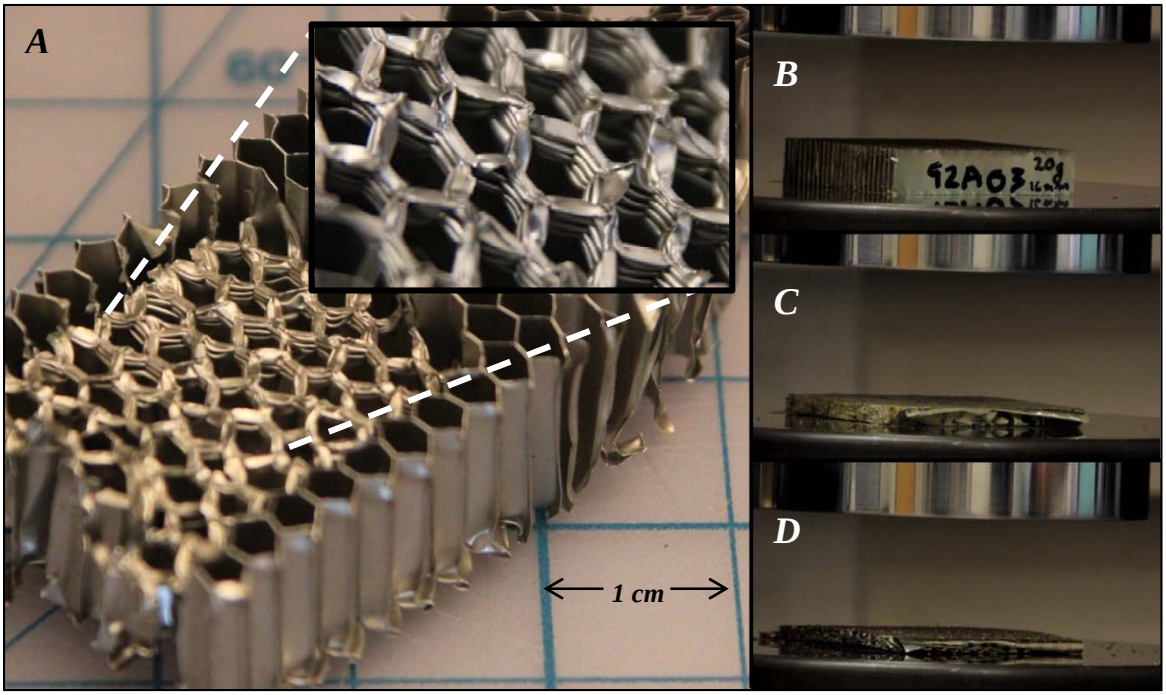

Figure 21. (A) Aluminum honeycomb cells collapse in concertina-like manner; (B) treated test sample prior to compression, (C) and after compression; (D) untreated sample after compression showing less resilience in both compressive displacement and material cohesion.

increase the material's strength and its post-compression cohesion in that the compressed treated samples did not crumble into smaller bits of debris like the untreated honeycomb material. A plot of the testing results for four of the samples is shown in Figure 22, while a description of the modifications made to the honeycombs for these tests is listed in Table 3.

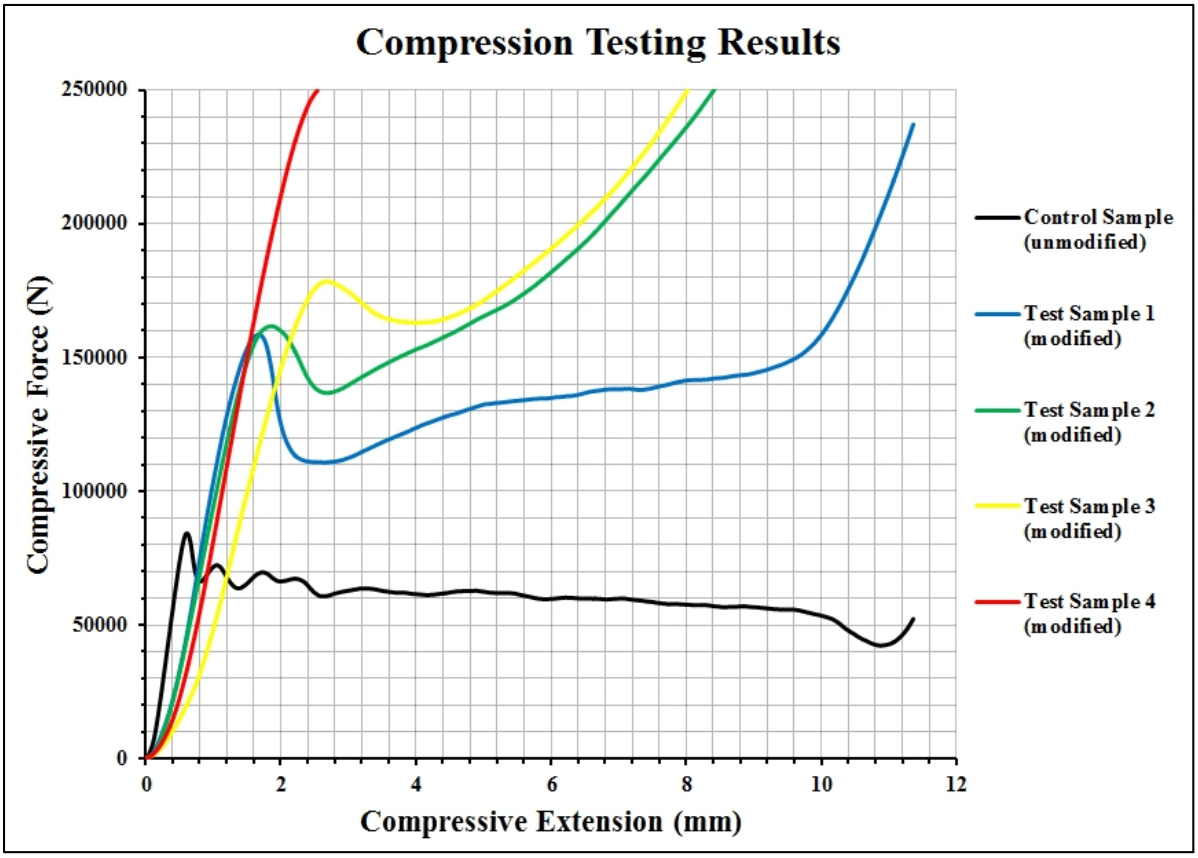

Figure 22. Comparative results from compression testing of four modified samples to the control sample. Sample 4 rapidly exceeded the Instron's loading capabilities; modified samples' behavior after reaching their initial yield threshold is very different from the control, rapidly increasing in strength as the material compresses.

Hexcel® Sample (75x75x16 mm)	Modification	Mass	Maximum Compressive Load
Control Sample	none	20 gm	84.31 kN
Test Sample 1	Kevlar Putty 25.4 mm spacing	45 gm	237.13 kN
Test Sample 2	Foam epoxy	34 gm	250.50 kN
Test Sample 3	Kevlar Putty 12.7 mm spacing	50 gm	250.64 kN
Test Sample 4	Kevlar putty 6.4 mm spacing	65 gm	(unknown)

Table 3. Sample modification descriptions, masses, and maximum compressive loads.

The addition of various fillers in the Hexcel® significantly increased the material's maximum compressive yield, and in most cases did not result in a substantial addition of mass. The material was integrated into the penetrator system to create a crumple zone (Figure 23) capable of protecting the SRC during impact, while a machined, solid nose cone allowed for adequate penetration.

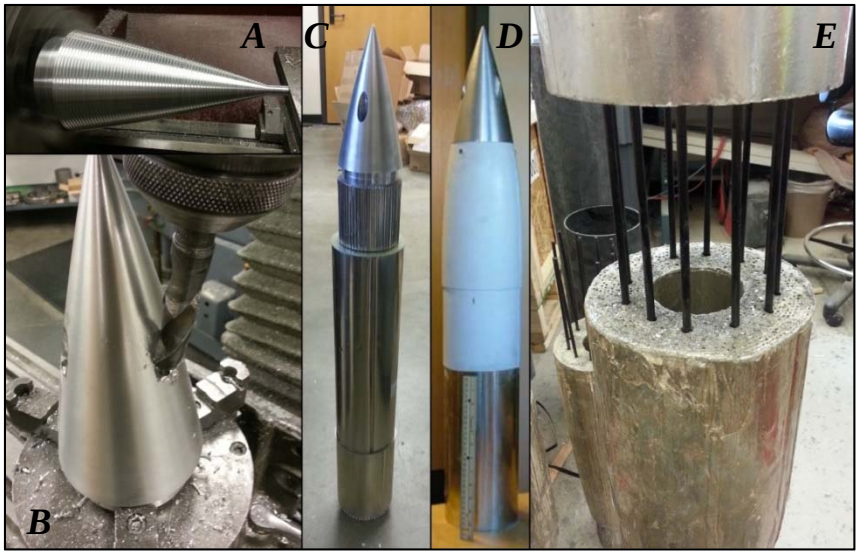

Figure 23. (A) Machining of the one of the Phase I aluminum nose cones, (B) and feed ports. (C) The nose cone and modified honeycombed aluminum, (D) and their integration into the rocket assembly. (E) Carbon fiber rods reinforced joints between sections of energy absorbing material to help resist shearing during impact.

Ensuring adequate penetration depth not only requires sufficient impact velocity, but also that the nose cone of the penetrator is at least as hard as the target material. During the NIAC Phase I study, impact modeling with ANSYS software was conducted to test the predicted worse-case scenario in which an aluminum nose cone embedded in material of similar hardness. A 15 cm block of Teflon was modeled as the target material for a 30 cm aluminum 6061-T6 nose cone (Rockwell hardness ~60 for both materials) impacting at 700 m/s [Winglee et al, 2013]. Figure 24 shows that while the nose cone experiences a fair degree of deformation during the impact, the feed port remains open allowing the continued flow of material into the collection system.

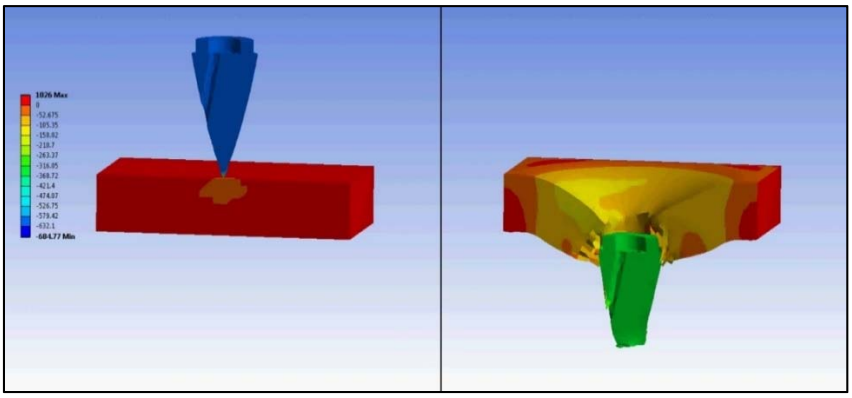

Figure 24. ANSYS modeling of a 700 ms^{-1} impact between an aluminum nose cone and Teflon block, color contours indicated speed of the object; simulations by Michael Pfaff [Winglee et al, 2013].

Since the target material in Phase I was playa, aluminum was determined to be sufficient for field testing; two nose cones were designed to test the differences in penetration depth for

different nose cone masses and geometries. Phase II testing required harder material for embedding in various soils and sandstone, so A2 Tool Steel was selected due to its relative ease in machining and its ability to be hardened to a Rockwell hardness ~62c. Additional design changes to the feed port geometry were made: one nose cone retained the triple, concentric feed ports, while the other employed a single feed port bored along the centerline of the nose cone. Figure 25 displays the four different nose cone designs.

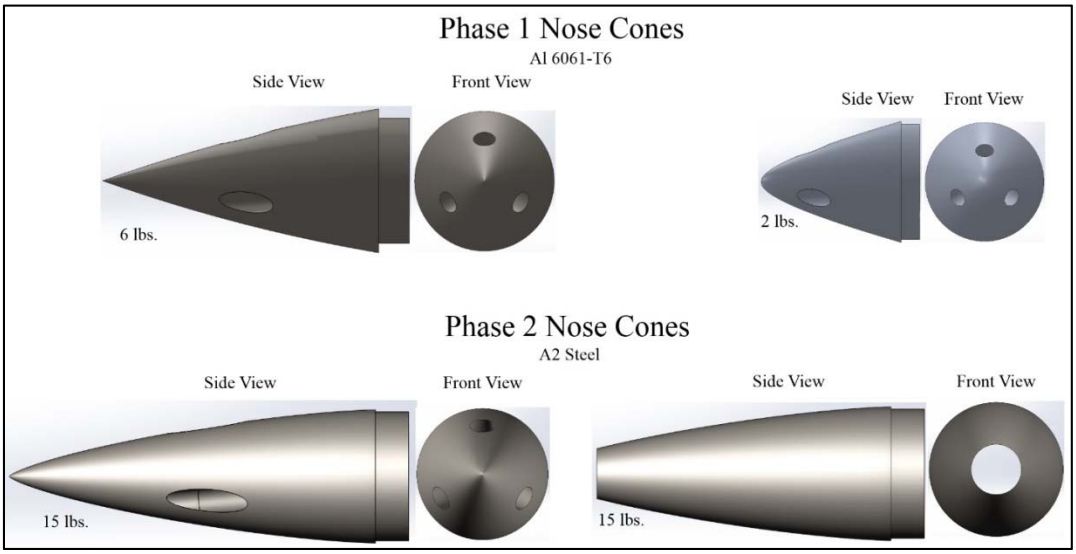

Figure 25. Comparison diagram showing the nose cone design for NIAC Phase I and Phase II.

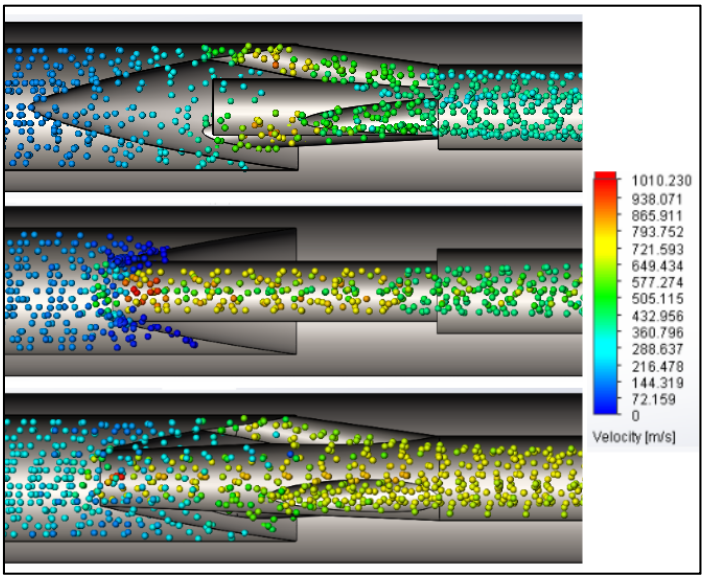

Figure 26. Relative flow model created in SolidWorks comparing the flow velocities between three feed port designs: the triple-port design (top), the single center port design (center), and the hybrid design (bottom). Relative flow velocity in the feed chimney is highest in the hybrid design; particle color designates velocity.

During field testing, the flow of incoming sample material was experiencing a stagnation point shortly after entering the feed chimney (see section 3.4). SolidWorks' FloXpress Analysis Wizard was used to model flow velocities inside the nose cones, and results of these models is shown in Figure 26. A new nose cone design was created that combined two earlier iterations resulting in a hybrid feed port configuration: a single, tapered centerline port, and three off set ports. It is important to note that solid material flow cannot be modeled in SolidWorks; instead, water was selected as the medium to demonstrate relative differences in internal flow velocities occurring in the three variants. Regardless, the modeling demonstrated the hybrid design allowed for the highest internal flow velocities. As such, a fourth evolution of the nose cone was produced, integrating the hybrid steel tip for penetration strength, with aluminum components to keep the final nose cone mass down. The fourth evolution can be seen in Figure 27.

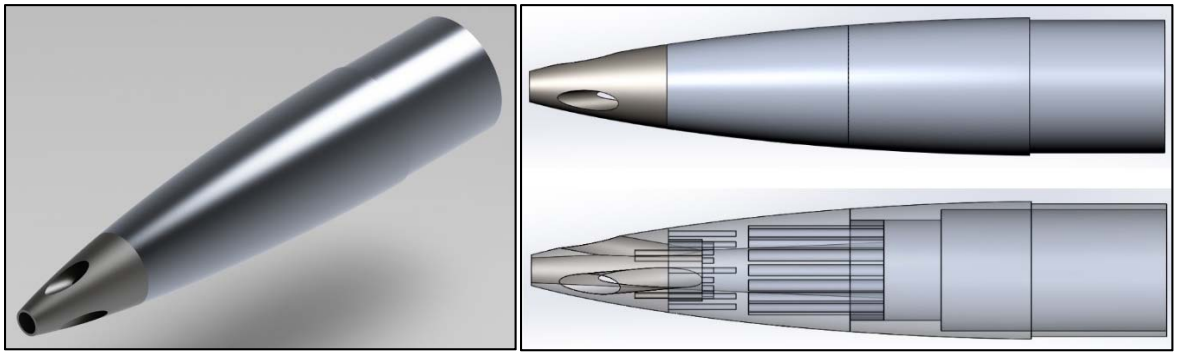

Figure 27. The fourth evolution of penetrator nose cones, integrating a steel tip using the hybrid feed port design, with two aluminum section tapering up to the full diameter of the rocket.

Planetary penetrators using methods proposed in the SaRSEE concept require no propellant since they utilize momentum imparted from the spacecraft, and aeronautical concerns are minimal since primitive bodies have negligible atmospheres at best; however, testing penetrators on Earth require both propulsion and aerodynamic stability to reach the desired impact velocities. During the NIAC Phase I study, a two stage, inline motor design was tested in the Black Rock Desert. The boost stage was designed to lift the vehicle to apogee at about 1,500 meters, and separate from the second stage. The vehicle was then allowed to free-fall for about 200 meters to achieve near-terminal velocity before igniting the second stage motor, providing aerodynamic stability prior to ignition to ensure both a reasonable impact angle and to lower the risk posed to ground operations crews. Optimized tail fins provided passive stability during flight, and aerodynamic drag was reduced by covering the feed ports with layers of carbon fiber. Figure 28 shows a schematic of the Phase I system. The problem with the Phase I design though was that the inline second stage motor could not be ejected prior to impact and its momentum ended up destroying the sample return system. A kite and balloon lift system were also examine and are viable for Mach 1 penetrators but as we moved to investigate speeds close to Mach 2, the weight of the motors and the fully reinforced penetrator became too heavy for these types of light system.

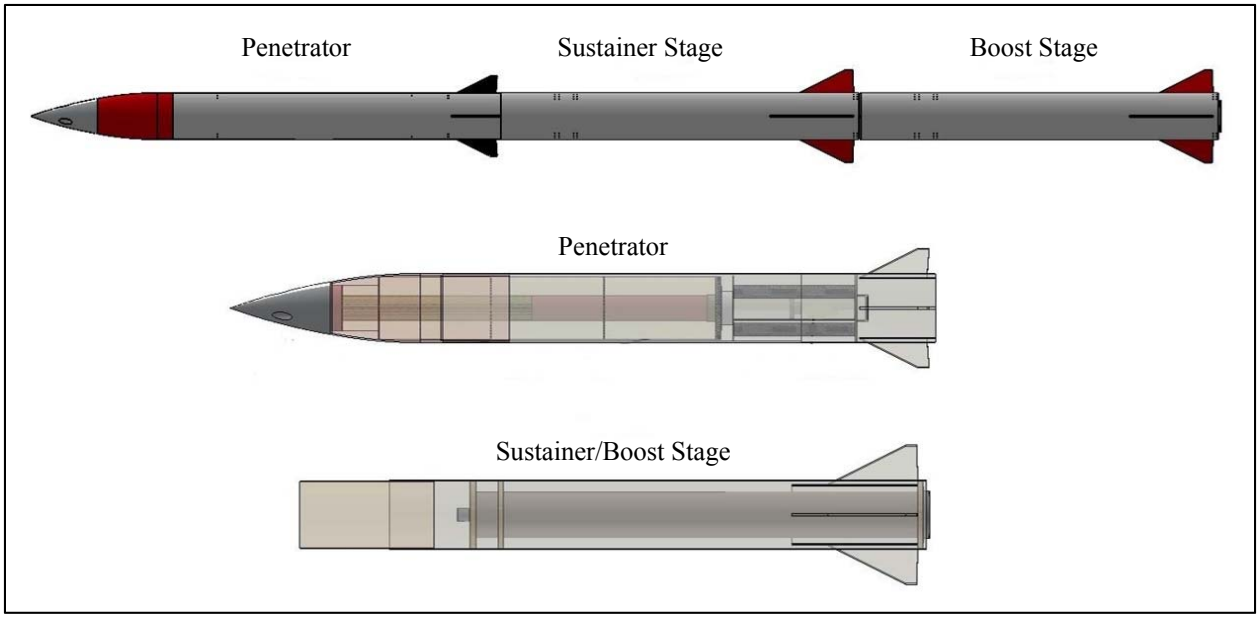

Figure 28. The NIAC Phase I, two-stage penetrator.

During NIAC Phase II, advances with clustered motor stages allowed for the redesign of the penetrator. Instead of a single, in-line motor, eight out-board motors were incorporated, reducing the overall length of the rocket. The out-board motors were integrated directly into the airframe of the penetrator and were designed to shear off during impact, preventing the motor casings from following the penetrator along the embedding vector. ANSYS simulations were created to confirm the design evolution prior to field testing; Figure 29 shows the updated penetrator design, and Figure 30 shows images from the modeling demonstrating the motor casings shearing off during impact. The system is capable of speeds at impact of about Mach 2 and able to penetrate 6 ft of concrete while attaining overall integrity of the feed system during the impact. Because of their ability to cut through 6ft of material the series of prototypes developed under the program were called “Gravediggers”.

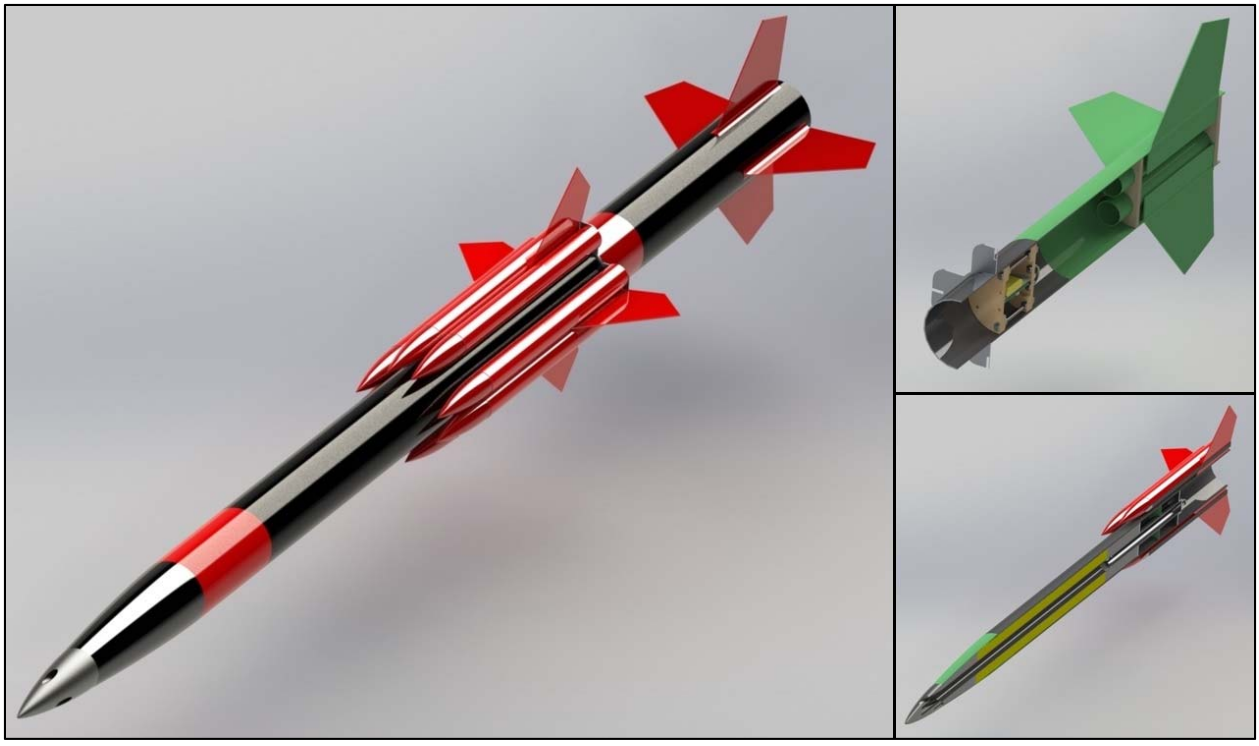

Figure 29. The NIAC Phase II, two-stage penetrator showing the out-board motors, and cutaway views of the boost stage and penetrator; the sustainer stage was integrated directly into the penetrator airframe.

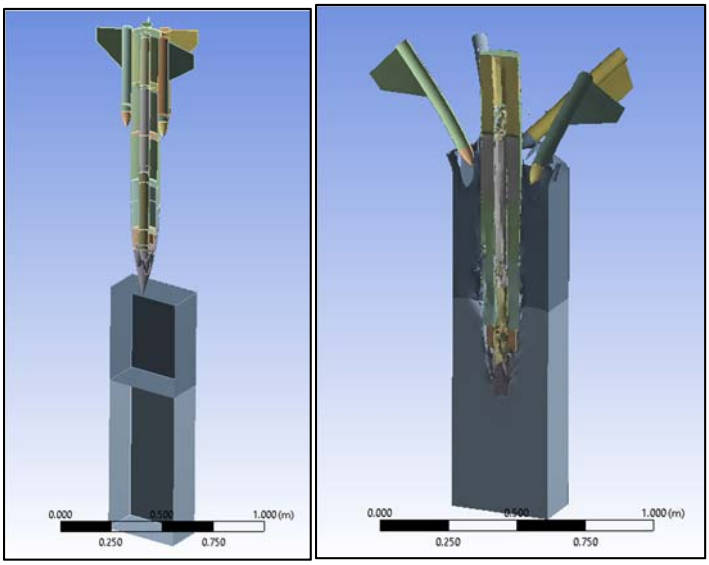

Figure 30. ANSYS modeling of the Phase II penetrator showing the out-board motors shearing off during impact; simulations by Michael Pfaff.

8. Field Testing

The process of moving from theoretical design to testing concepts in the field inherently reveals flaws in assumptions made early in the process, and professional aerospace organizations

may spend years and millions of dollars refining a product to develop a finalized, fully functional system. Time and budgetary constraints of the NIAC Phase I and Phase II studies allowed for only a precursory evaluation of the SaRSEE mission proposal, dominated by the proof-of-concept for the penetrator, and as such there remains extensive development needed for moving beyond Technology Readiness Level 3. Despite these limitations, the research conducted over the course of three years did in fact demonstrate the potential for the use of penetrators for sample return, and the following sections review field testing conducted for the Phase I and Phase II studies. Amateur rocketry methodologies adopted from the University of Washington's Department of Earth and Space Sciences rocketry program allowed for the rapid, in-house production of the penetrators to facilitate their fabrication under the NIAC financial, and scheduling requirements. The dependence on cheap, commercially available propellant and passive stability systems often produced unexpected results, to say nothing of the challenges involved in finding suitable (and legal) areas for conducting the tests. The resilience and perseverance demonstrated by SaRSEE team members in meeting these trials head-on embodies the best of what NIAC aspires to in challenging the status quo in current aerospace practices, finding innovative solutions to seemingly unconquerable obstacles, and revolutionizing the approach to space exploration.

8.1. Phase I at Black Rock, Nevada, March 2013

Initial testing for the SaRSEE penetrator was conducted during the annual trip to Black Rock, Nevada, for the Rockets & Instrumentation course offered by the University of Washington's Department of Earth and Space Sciences. Figures 30 through 34 represent only a portion of the work conducted during Phase I; for a full review of Phase I results, refer to the final NIAC report, "Sample Return Systems for Extreme Environments" [Winglee et al, 2013]. These initial flight tests of the penetrators demonstrated our ability to perform high velocity impact testing. Survivability of the impact was demonstrated to be possible at a moderate speed of Mach 0.5 so that we were able to go from the ramble pile of the crash that inspire the proposed efforts to a fully intact penetrator system going into the ground at the same speed and ground material. However, the design for higher speed impacts was found to be lacking the usage of inline motors as described in Section 6.

Despite the design issues with the launch system, the Phase I results did demonstrate that material could be moved into the central feed system through the energy of the impact, and the Phase II results bellow show the evolution of the system to the point where self-ejection of a core sample from a high velocity impact becomes possible.

Figure 30. (top) The first SaRSEE penetrator, Gravedigger 1, just prior to being loaded on the launch rail. The rocket employed an Aerotech M1850W (7,500 N-sec) in its black boost stage, and an in-line, Cesaroni N10,000 (10,347 N-sec) motor in the purple sustainer. (bottom) RockSim software was used to create flight simulations for all field tested penetrators, showing the acceleration, velocity, altitude, and the flight angle of the sustainer. Oscillations in the flight angle of the sustainer represent hunting behavior indicative of velocities too low for passive aerodynamic stability; as velocity increases, the rocket stabilizes before the ignition of the second stage.

Figure 31. (A) During the flight of Gravedigger 1, the second stage motor casing failed during ignition when the forward enclosure sheared off. While the penetrator was blown clear, the resulting impact velocity was lower than desired (~180 m/s). (B) The impact created a clearly defined crater, with radial fractures in the playa, (C) and the penetrator embedded to a depth of 1.32 meters at an angle of ~30° off normal. (D) Post recovery examination of Gravedigger 1 revealed the impact resulted in almost no internal damage to the penetrator, but the impact velocity was too low to open the feed ports that had been covered with carbon fiber, so no sample was collected.

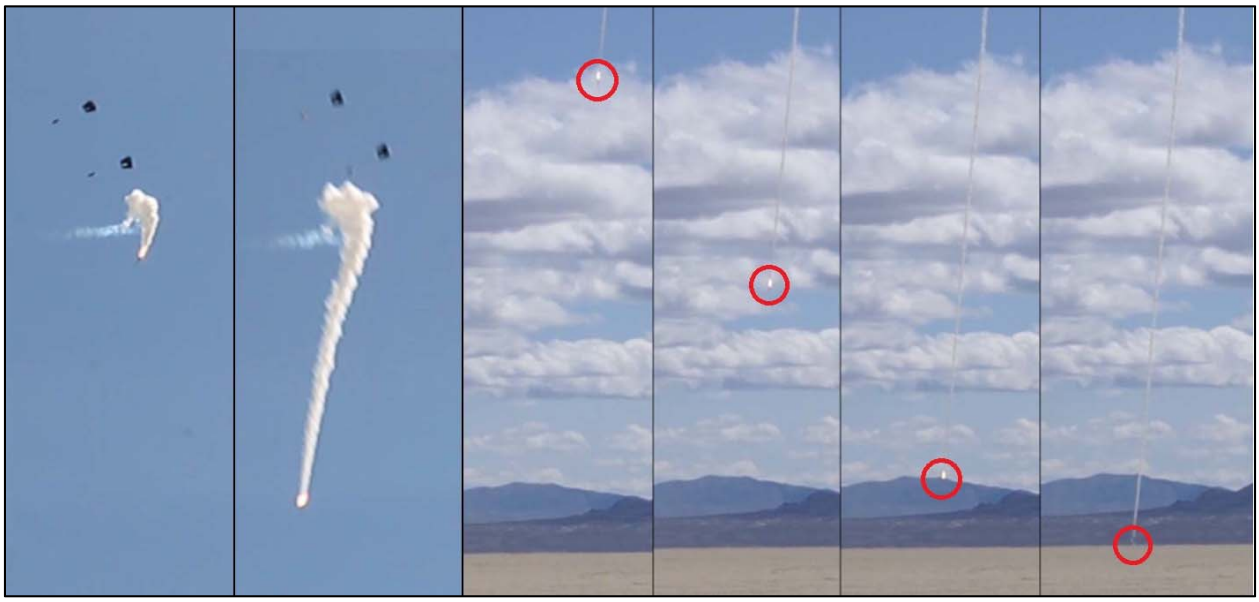

Figure 32. Gravedigger 2 was lifted to launch altitude by two power sled kites then used the motor ignition to instantly sever its connection to the kites, reaching an impact velocity of ~420 m/s [Winglee et al, 2013].

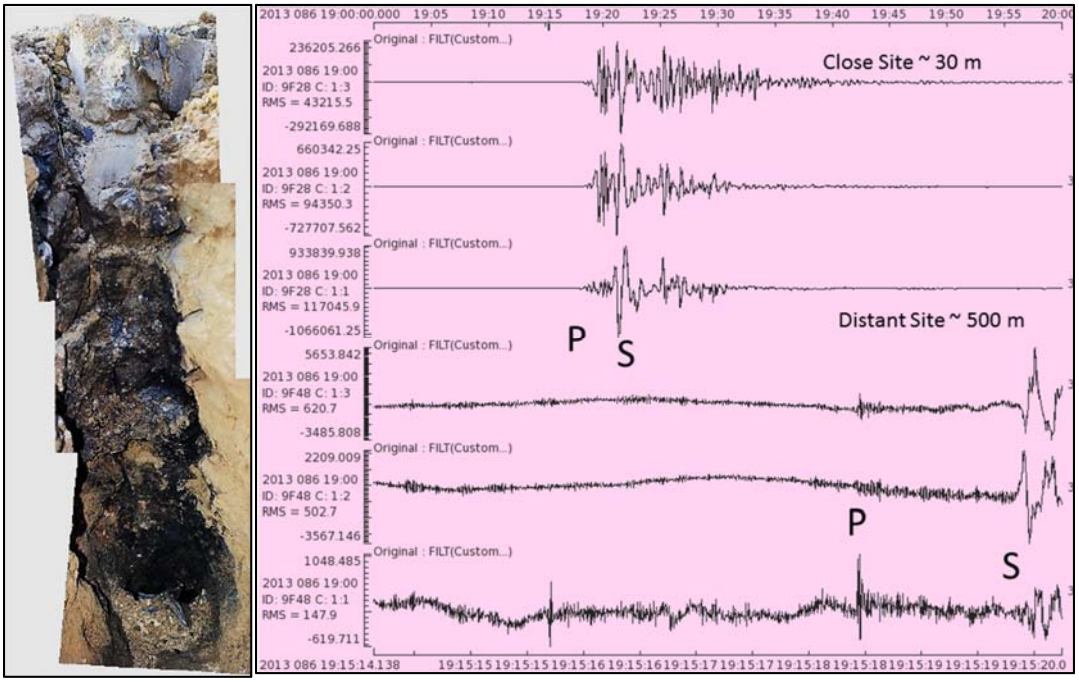

Figure 33. Limitations in the available tether used during testing of Gravedigger 2 resulted in the penetrator embedding while still under power; the resulting impact embedded the penetrator to a depth of ~2.13 meters, but the majority of the rocket was destroyed by the still-burning fuel grains. Seismometers placed at two different sites captured the impact, and the resulting P and S waves [Winglee et al, 2013].

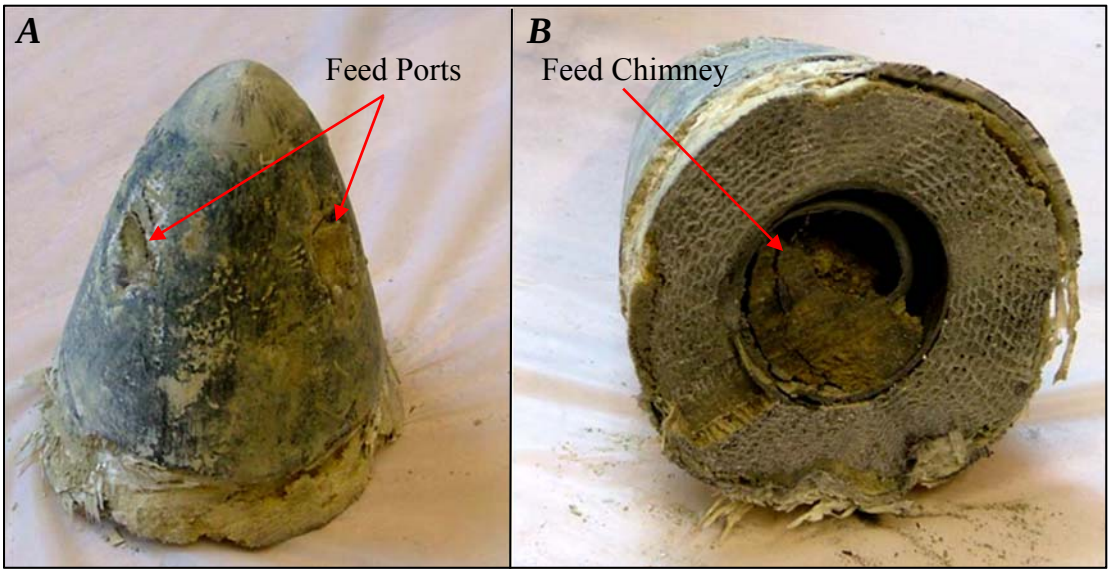

Figure 34. While much of the penetrator did not survive the impact, Gravedigger 2's nose cone successfully demonstrated the concept of the collection of material via the feed ports. (A) Carbon fiber covered feed ports opened during impact, allowing material to flow into the feed chimney; (B) when the nose cone was dissected, ejecta was firmly packed inside the feed chimney where the only available path was through the feed ports [Winglee et al, 2013].

8.2. Phase II at Naval Air Weapons Station, China Lake, June, 2014.

As was mentioned in Section 2.3, advances in the program with the application of clustered motors allowed for a redesign of the system by integrating clustered motors directly into the penetrator's airframe, eliminating the need for a separate sustainer stage. Concerns about the ability to maintain a secure test site at Black Rock resulted in moving field tests to the Naval Air Weapons Station (NAWS), China Lake, California. Despite efforts to demonstrate the ability to safely conduct the testing using a ground-launched, two stage system, NAWS range personnel were unwavering in their instance on a single stage system.

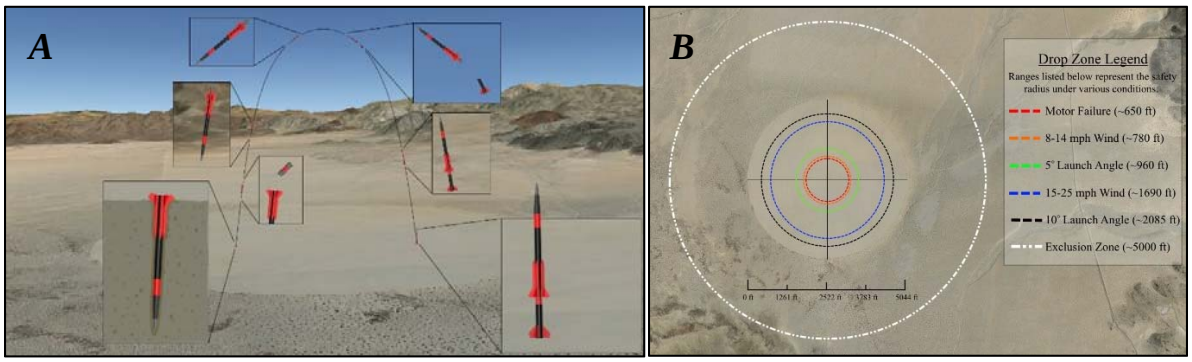

Figure 35. (A) Flight plan schematic produced for NAWS describing the use of the ground-launched, two stage penetrator system. (B) Dozens of flight simulations were created using RockSim to determine the kinetic footprint for the testing; alterations to the launch angle and wind speed were made to create range estimates. Additionally, progressive motor failure in the penetrator stage were simulated, and ultimately the simulations suggested high wind speeds and launch angles were more likely to increase the rocket's range than motor failures creating non-symmetric thrust in the penetrator stage.

To comply with NAWS concerns, a new flight plan was conceived and executed using clusters of tethered sounding balloons to lift the penetrator stage to altitude, ensuring the rocket constantly pointed down into the drop zone. Unfortunately, launch times were restricted to poor times of the day where extreme temperatures, and high winds proved to be beyond the endurance of the sounding balloons, all of which burst prior to lifting any payloads. Efforts were made to attempt a ballistic drop of a lightened penetrator using the power sled kite method demonstrated in Black Rock the prior year, however restrictions limited the flight to using only one insufficient lift. Ultimately these setbacks prevented any penetrator launches at NAWS.

Figure 36. UW researchers and volunteers pose at NAWS with Gravedigger 3 and 4 added in the foreground.

8.3. Phase II : 1st Field Testing at Ione, CA, December, 2014.

Continued testing at NAWS was financially and technically prohibitive, so an alternate test site was arranged that allowed the ground team greater flexibility, while maintaining a small kinetic footprint. Through serendipitous meeting at the Annual NIAC meeting, we made contact with a rancher in Ione CA whose site was used for some of the experiments in the program *Myth Busters,* and would allow the penetrator testing to occur but restricted in winter and early spring when the fire danger was low during the persistent drought in CA.

During the first campaign, testing emphasis was placed on refining the clustered motor methods with a newly developed, student-built flight computer. The first flight was designed to test both the clustered boost stage's capability, and the post-apogee separation required for a fully powered test where the penetrator's airframe would also be equipped with clustered motors to maximize impact velocity. During the first launch, two of the four motors in the boost stage failed to ignite; however, the failed ignition was symmetric, allowing a clean launch but resulting in a lower apogee than anticipated. The new flight computer also failed to separate the boost stage, but despite the anomalies the penetrator embedded nearly normal to the surface with an impact velocity of ~200 m/s (Figure 37). The target material consisted of about 0.61 meters of packed soil, overlying a variety of river stones deposited by a near-by stream that had migrated west over the span of time.

Figure 37. (A) Initial results of clustered, boost stage test using the single, centered-bore, steel nose cone; (B) the penetrator embedded to a depth of ~0.86 meters.

Post-recovery analysis of the penetrator revealed the steel nose cone sustained no significant damage during impact, but sample collection did not occur as hoped. Upon examination, the flow of incoming material appeared to stagnate roughly 0.33 meters after entering the feed port (Figure 38). During the impact, sample material becomes compressed by the impact pressure until its failure threshold is exceeded, at which point it behaves in a fluid-like manner; however, as the depth of penetration increases, velocity and pressure decrease and the initial compaction relaxes and the material behaves more elastically and expands inside the feed chimney. This behavior was also observed following the analysis of the third penetrator of the campaign, even with a different feed port geometry.

Figure 38. (A & B) The center-bored feed port, steel nose cone sustained no significant damage; (C) measurements made through the aft of the penetrator suggested material flow had stagnated around 0.33 meters after impact; (D) the penetrator in cross-section, showing the stagnated material inside the feed chimney; (E) close-up of the stagnation point with remnants of the feed port cover (pink shell fragments) mixed in the ejecta.

The use of commercially available, amateur motors allowed for relatively inexpensive testing, but inconsistent motor performance created many difficulties during this campaign. The second attempt in the application of a clustered boost stage resulted in only one of the motors coming to pressure as the rocket left the launch rail. Under this one motor the rocket tilted at about 100 ft where addition motors came up to pressure causing the rocket to clear the launch rail but failed to exceed 100 feet in altitude before losing power. The rocket landed horizontally and was expected to be a total loss, but upon inspection the penetrator had remained intact with only the boost stage and coupler sustaining damage.

The decision was made to load the penetrator airframe with four motors and attempt a ballistic impact, since all the propellant would be consumed during launch. This second attempt again experienced ignition difficulties, with one of the four motors lighting at launch, followed by the remaining three igniting nearly two seconds after the rocket left the rail. These ignition problems resulted in the penetrator accelerating along a horizontal trajectory, embedding at a shallow angle in a near-by hill side (Figure 39). Impact velocity was estimated to be ~330 m/s, penetrating through ~1.8 meters of packed top soil, and while not a total success the flight did validate modeling results that showed the outboard motor tubes shearing off during impact. Impact velocity was sufficient to open the covered feed ports but sample material stagnated in the feed chimney as it did in earlier impacts, so the bulk of the material did not reach the SRC;

however, the backflow baffle did in fact collect lighter ejecta that traversed the length of the penetrator (Figure 40).

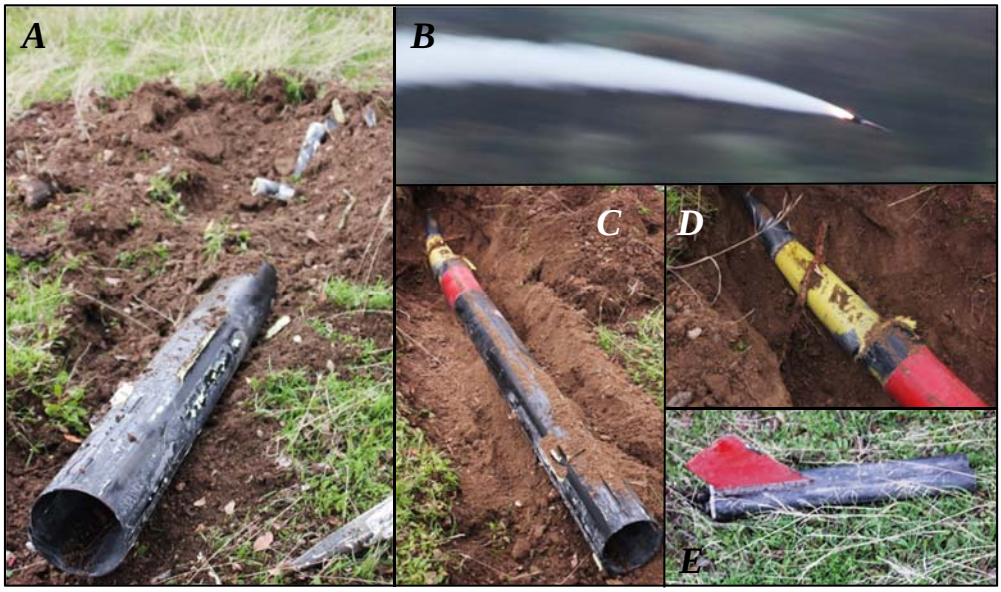

Figure 39. (A) The penetrator embedded at a shallow angle into the hillside, with nose cones from the motor tubes that sheared off seen in the impact ejecta; (B) ignition problems resulted in the penetrator taking a horizontal trajectory; (C) the penetrator embedded through ~1.8 meters of packed top soil; (D) spiral fracturing occurred in the aft portion of the nose cone during impact, but micro-failures in the fiberglass may have been created during the prior launch failure; (E) one of four pairs of motor tubs that sheared of during impact as designed – this pair was located about 8 meters uphill from the impact site.

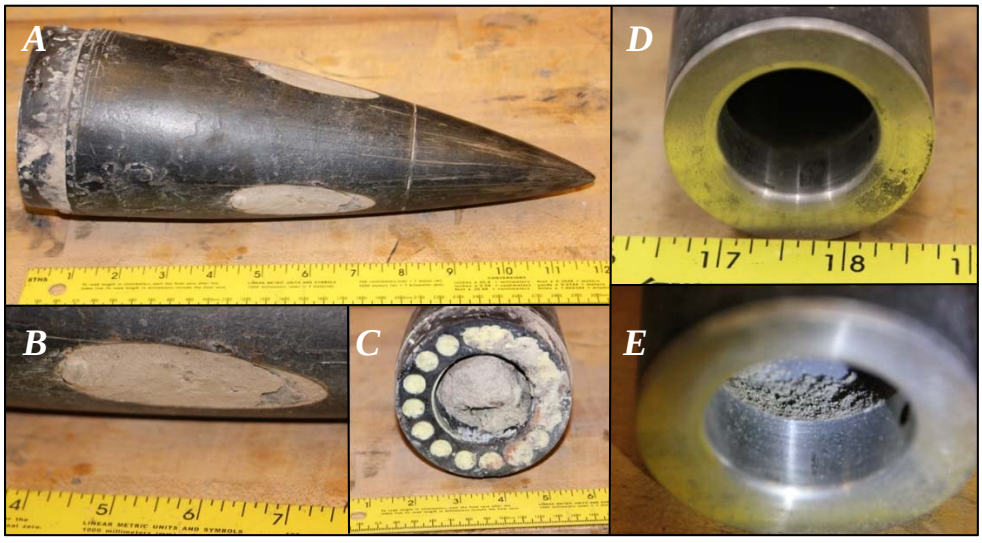

Figure 40. (A) The nose cone experienced no deformation during impact, (B) and feed ports opened successfully. (C) Ejecta experienced stagnation at the start of the feed chimney; (D) the backflow baffle inside the SRC successfully collected fine ejecta (E) that traveled through the feed chimney.

The final flight of the campaign (Gravedigger 3) used the old design of the penetrator system from Phase I as it was the backup system in case launch anomalies were experience. This flight has no ignition anomalies, and successfully demonstrated the clustered, two-stage flight concept (Figure 41). The flight also demonstrated the importance of having a nose cone that is harder than the target material. Impact velocity was

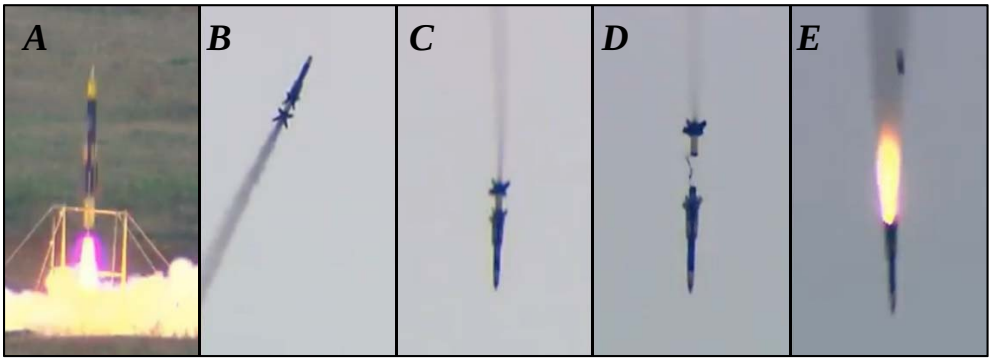

Figure 41. (A) Successful ignition and launch of the clustered, two-stage penetrator; (B) burn-out of the clustered boost stage as the rocket cruises to apogee; (C) post-apogee free fall, allowing the rocket to reach aerodynamic stability before igniting the second stage; (D) separation of the boost stage; (E) ignition of the second stage showing the separation of the inter-stage coupler, containing the flight computer, that was fitted with blast plates to facilitate separation upon ignition of the second stage.

estimated to be ~450 m/s, and the penetrator embedded to a depth of ~0.9 meters, having encountered a softball-sized piece of quartzite. The impact deflected the aluminum nose cone, resulting in the penetrator taking a cork-screw like path (Figure 42). While the SRC survived intact, the twisting of the rest of the penetrator prevented sample material from traveling up the feed chimney. The most encouraging feature was that the sample return canister (SRC) was found close to the surface.

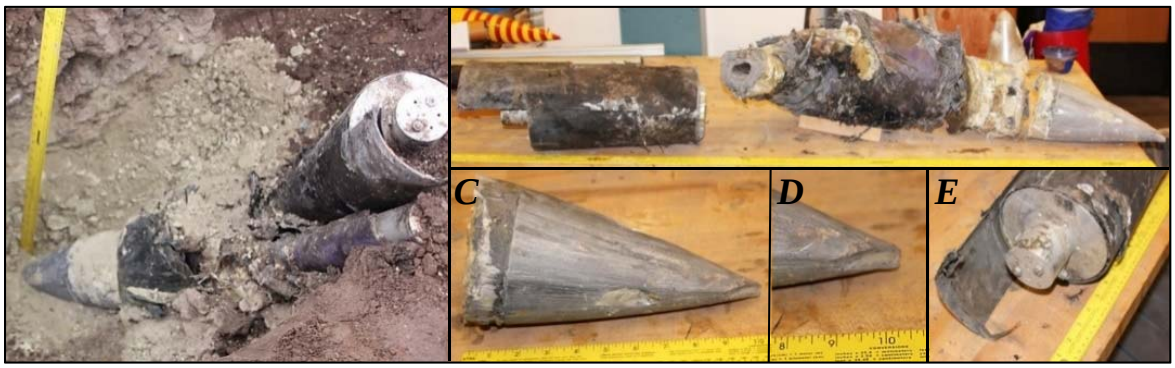

Figure 42. (A) The penetrator embedded to a depth of ~0.9 meters, but was deflected off a straight trajectory when it struck a piece of quartzite; (B) the deflection resulted in massive deformation of the penetrator that separated the body at unreinforced seams in the energy absorbing core material, and prevented sample material from reaching the SRC; (C) the aluminum nose cone experienced some deformation during the impact, although the feed ports remained open; (D) the contact point where the nose cone encountered the quartzite; (E) the SRC remained intact, but warping in the airframe resulted in binding.

8.4. Phase II : 2nd Field Testing at Ione, CA, March, 2015.

The second campaign of penetrator tests outside Ione took place at the end of March, 2015, and while commercial motor issues continued to cause complications, the series resulted in a Mach 2 impact into sandstone (Gravedigger 4). Drawing lessons learned during the first Ione campaign, the nose cone was redesigned in an effort to mitigate the stagnation issues found with earlier iterations (section 2.3). Combining the feed port configurations – three, off-set feed ports, and a large, single, concentric feed port – in a new hardened steel tip increased internal flow velocities, while mating the tip to an aluminum extension resulted in an assembly with a mass similar to earlier evolutions. The penetrator was fitted with a full array of eight, outboard motors to provide the highest impact velocity following the post-apogee free fall, and a clustered boost stage was selected for launch after discovering critical components for a large single motor boost stage had not been included with the fuel grains. Slight ignition timing delays in the boost stage resulted a launch angle of ~30°, reducing the ideal apogee altitude to ~3,000 feet. While this reduced the planned free fall time, the rocket remained stable during the ignition of the second stage and produced a very loud sonic boom, immediately followed by the sound of the impact. Impact velocity was estimated to be over 600 m/s, embedding to a depth of 1.6 meters into solid sandstone.

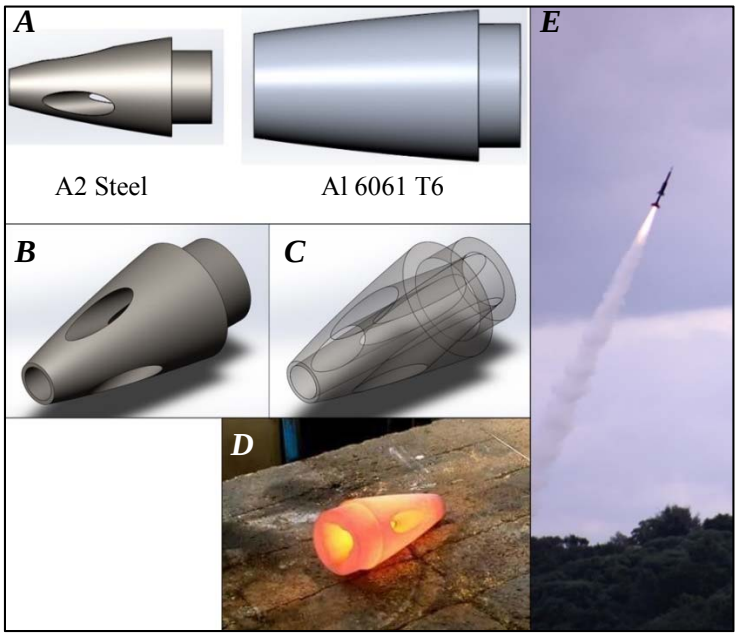

Figure 43. (A) The steel and aluminum components of the third evolution of penetrating nose cones; (B) the hybrid steel nose cone exterior; (C) transparent view of the hybrid design showing the confluence of the four feed ports; (D) the steel tip after initial heat treating; (E) the penetrator equipped with the hybrid nose cone accelerating toward apogee.

Rocket/Motor debris from the penetrator was spread across a broad swath of the hillside (Figure 44). The impact crater showed less surface disruption than observed in other tests, and only a limited ejecta fan. An important result was that both the attachment bracket and the top of the return sample canister was found above the surface at 0.5 and 83 m respectively from the impact site, impacting that there is impact energy available to produce ejection of the SRC.

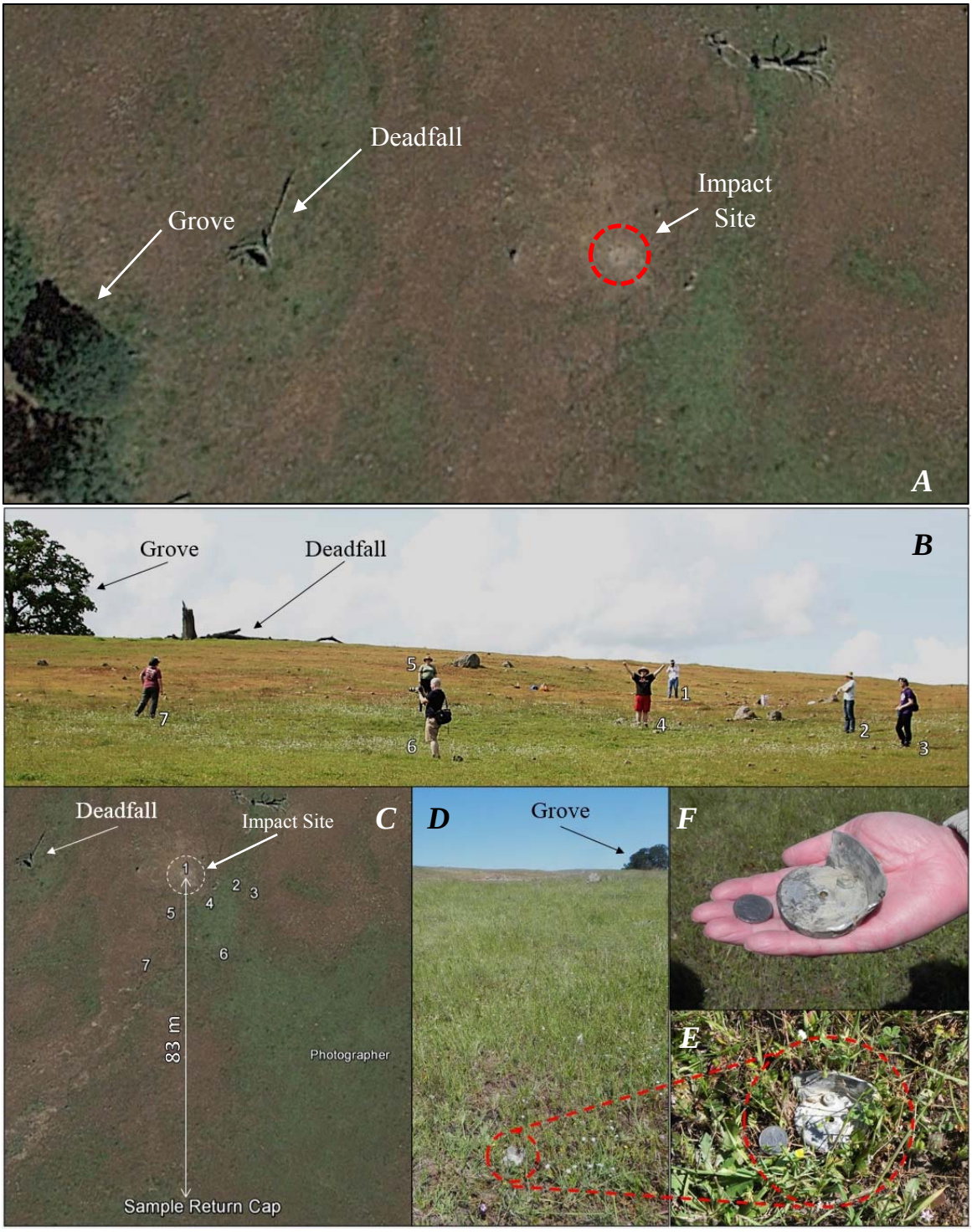

Figure 44. (A) A Google Earth view of the impact area taken just a few weeks after testing; (B)students and researchers stand next to pieces of debris larger than six inches – mainly sheared motor tubes - where numbers reference positions; (C) the approximate positions of researchers and students marking major debris, some of which fell more than 80 meters from the impact site; (D)(E)(F) the Sample Return Cap was ejected during the impact, but uncertainties remain if the ejection was due to refractory waves traveling through the system, or rapidly increasing internal air pressure created in the SRC during the impact.

Once the top few inches of soil was removed, the underlying sandstone was revealed and the impact shaft contained a large amount of backfill. Loose backfill debris was removed revealing the top of the impact shaft, 4 inches in diameter, with clearly observable slickensides (Figure 45). Recovery of the penetrator took more than a total of 10 hours, with crew members carving out shoe-box size blocks of sandstone with hand tools. Earlier impact models suggested that material proximal to the impact shaft would experience varying levels of fracturing; however, observations made during the excavation of the penetrator did not validate the predicted response. Instead, the rocket created a shaft with a diameter that matched the maximum diameter of the metal portions of the nose cone assembly of 4 inches (where as the main body of the penetrator had a six inch diameter), with no observable fracturing of material adjacent to the shaft.

Figure 45. (A) The surface of the impact site exhibited a limited ejecta fan (less than 1.8 X 1.8 meters), with some material overturn, and fracturing of the sandstone around the impact shaft isolated to the top few inches near the surface, the SRC attachment bracket was found above the surface (red circle); (B) backfill debris filling the 4 inch diameter impact shaft highlighted by the red circle; (C) once backfill was removed, slickensides indicative of penetrator embedding aligned along the impacting vector; (D) recovery crews spent more than ten hours removing blocks of sandstone with hand tools, excavating to a depth of 1.6 meters.

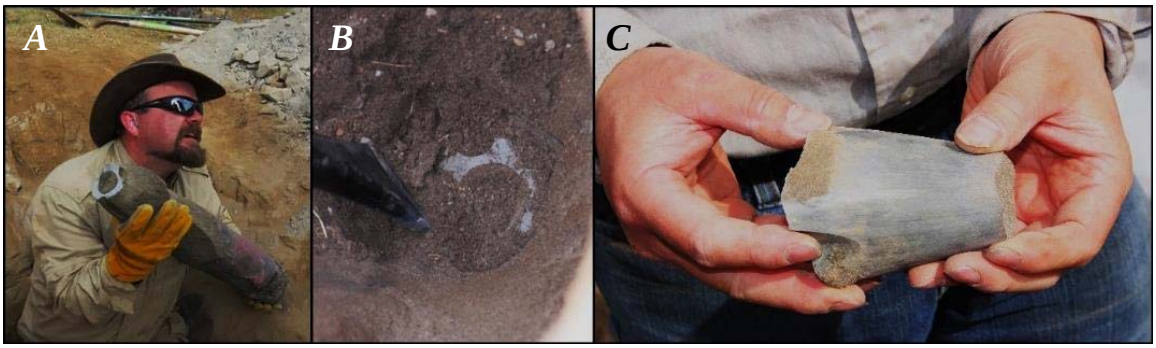

Figure 46. (A) The removal of the main body of the penetrator; (B) forces during the impact resulted in a brittle failure three inches aft of the front of the steel tip, leaving the separated portion embedded in the sandstone after the main body of the penetrator was recovered; (C) the recovered steel tip.

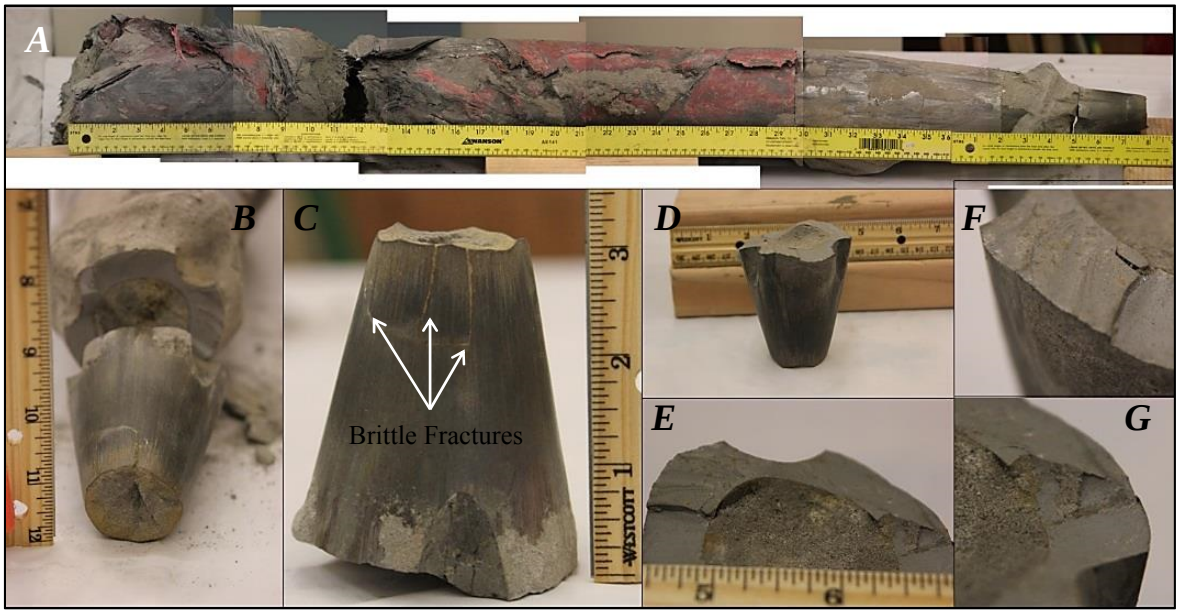

Figure 47. (A) Composite images showing the recovered penetrator – note the large fracture 1 foot from the aft of the penetrator and the increasing diameter of the body; (B) the steel tip fractured about 3 inches from the forward end but the fracture plane exhibited no evidence of impact material coming between the separated portions, suggesting the failure occurred either at the very end of the impact, or only separated from the main nose cone during recovery; (C) the front of the center feed port experienced some brittle fractures where the wall thickness was very thin (<.125 inches); (D)(E)(F)(G) it was initially suspected that the failure plane had originated at the three, off-set feed ports since the wall thickness at those locations was only ~0.25 inches, however the major brittle failure features occur where wall thickness was 0.5 inch. Material failure was likely the result of over-hardening of the steel (Rockwell hardness ~62c), instead of optimizing hardness and strength, resulting in a hard but brittle tip that still provided effective penetration and sample collection.

There was some fracturing and examples of over-turned strata near the surface of the impact site, but these effects were limited to the first few inches and were not observed at greater depths. The diameter of the main body of the penetrator was six inches, whereas the maximum diameter of the aluminum and steel nose cone assembly was four inches. Earlier modeling suggested that during embedding, material immediately proximal to the impact would experience significant fracturing during the impact, and in earlier tests into playa and soil there were observed stress fractures that had been created by the impact. The sandstone did not exhibit this behavior however, with proximal fracturing only observed near the surface where confining pressures from the surrounding rock were low. Characterizing the hardness of sedimentary rocks can be challenging and highly dependent on their mineral composition, and at the time of this report control samples had not been subjected to tri-axial compression tests so no quantitative values can be assigned to the sandstone; however, it is sufficient to recognize that the strength of the steel and aluminum nose cone was sufficient to penetrate through the formation, while the airframe and energy absorbing materials were not as resilient.

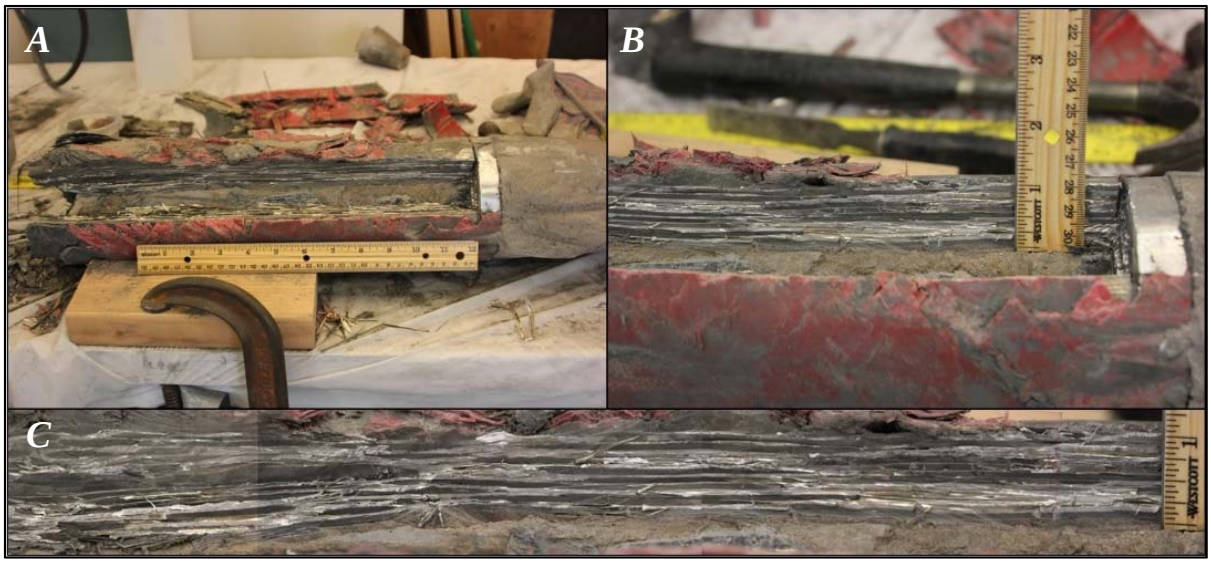

Figure 48. (A) The initial section of energy absorbing material compressed laterally instead of longitudinally, revealed after the first quarter of material had been dissected; (B) the six inch body diameter compressed to match the four inch diameter of the nose cone; (C) the energy absorbing material, consisting of honeycombed aluminum and carbon fiber rods, became a solid mass. Interestingly, while the aluminum cells had collapsed, the majority of the carbon fiber rods were found to be nearly intact even after the compression.

Since the adjoining sandstone did not fracture during the impact as predicted, the metal nose cone assembly bored an impact shaft four inches in diameter – the maximum diameter of the assembly. As the six inch diameter body embedded behind the metal nose cone assembly, the carbon fiber experienced spiral fracturing and was compressed laterally within the confines of the impact shaft. Simultaneously, sandstone collected through the feed ports traversed up the feed chimney to the SRC at a high velocity, creating large internal pressures on the inner

diameter of the energy absorbing material. Bound between high external and internal pressures, the honeycombed aluminum and carbon fiber material became compressed into a near solid mass, and was unable to compress along the intended longitudinal direction (Figure 48). This compressive behavior was consistent through the initial 18 inches of crumple zone, but then the material behavior changed.

Serious deformation began to occur after the initial section of crumple zone compression. While spiral fracturing continued up the exterior of the carbon fiber airframe, the section no longer continued to conform to the 4 inch diameter of the penetrator ahead of it. Over the length of the 12 inches of the section containing the SRC, the diameter tapered up to five inches, and when the outer inch of material was removed, severe deformation in the energy absorbing material and buckling of the SRC was observed (Figure 49). The section was then cut in half, revealing the extent of deformation experienced by the SRC. During the impact, sample material flowed at high velocity to about half the length of the SRC, but the pressures created caused the backflow baffle to turn 90˚ inside the SRC.

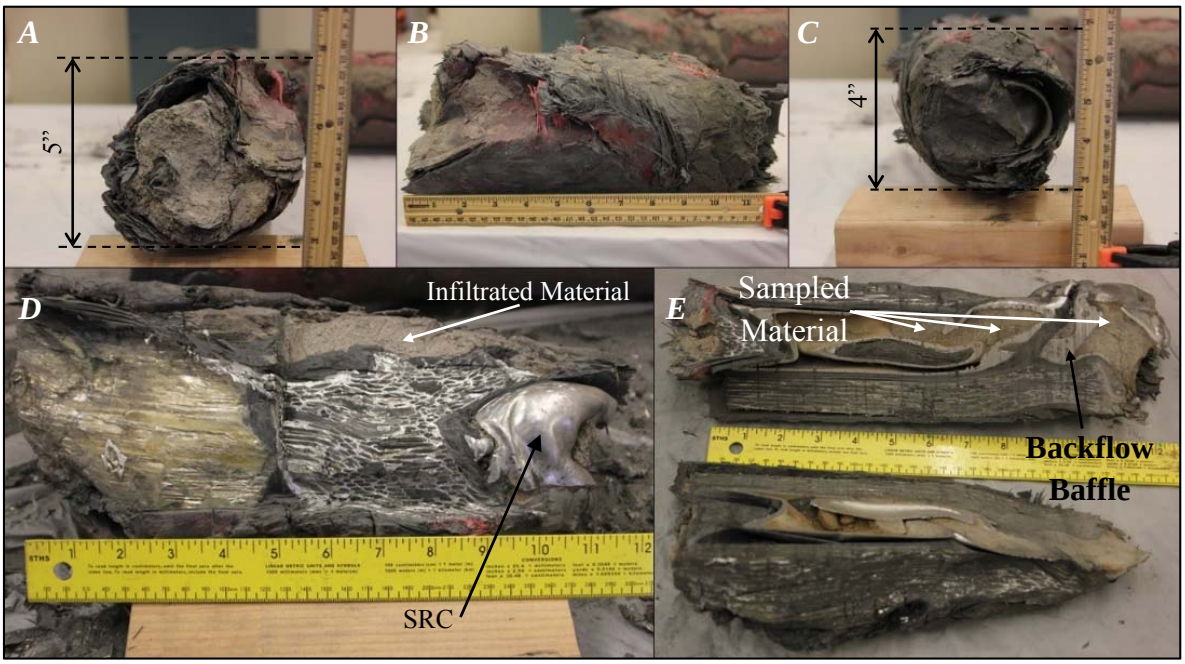

Figure 49. (A) The aft end of the crumple zone containing the SRC tapered up to a 5 inch diameter; (B) a side view of the section showing the increasing diameter; (C) the forward end of the section that began with a 4 inch diameter; (D) side view of the section following the removal of an exterior inch of material, showing massive deformation in the honeycombed aluminum, buckling of the SRC, and material that had breached the exterior of the section and did not come from inside the feed chimney; (E) when the section was cut in half, the full extent of deformation experienced by the SRC can be observed, showing sample material reaching nearly half the length of the SRC, and the backflow baffle dislodged and turned 90˚.

Without the internal pressure of material countering the exterior confining pressure, the SRC buckled and collapsed; the failure occurred after sample material had entered

the SRC, evidenced by the presence of sandstone beyond areas of severe deformation. Forces at work in the SRC resulted in the Sample Return Cap being ejected from the penetrator, coming to rest about 83 meters from the impact site (Figure 44).

Many questions remain concerning the behavior of the material during the impact, requiring further analysis. Clearly the design of the SRC was insufficiently robust, and new iterations are under development to increase its structural integrity, but it is unclear whether the deformation was the result of continued impacting momentum, or a result of refractory waves propagating through the system. Similarly, was the ejection of the Sample Return Cap the result of refractory waves, or the rapid expansion of the air column inside the SRC during embedding? How did the deformed section expand to a diameter of 5 inches, when the top of the impact shaft only exhibited a four inch diameter, and since this expansion occurred near the end of the impacting process, how does that inform the research concerning fracturing of the shaft immediately adjacent to the penetrator – fracturing that was not observed during recovery? One major take away from the test was that the maximum diameter of the metal nose cone assembly must match the diameter of the penetrator body; this seems obvious in retrospect, but since earlier impacts had not embedded in rock, this difference in diameter had not been an issue.

Figure 50. (A) The core sample was exposed after removing the encasing material; (B) note the swelling in the sample diameter near the aft end of the core, indicative of increasing pressures occurring forward of the section that experienced severe deformation.

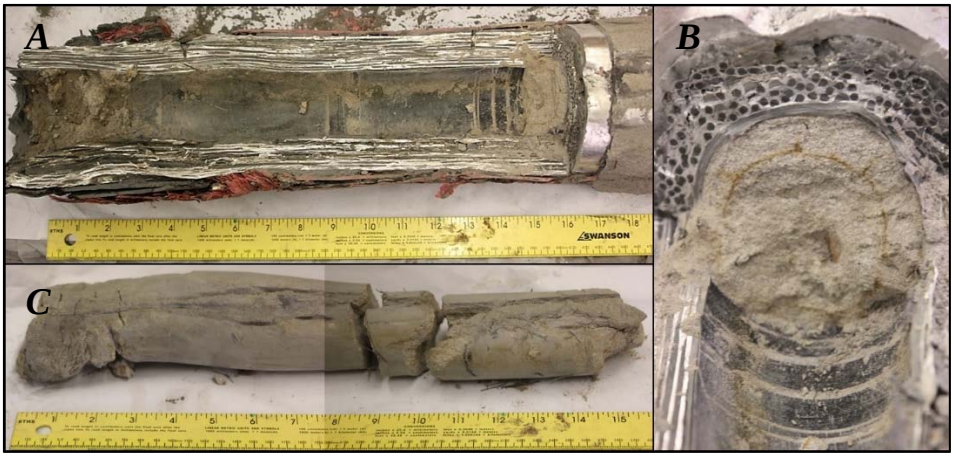

Figure 51. (A) The feed chimney after the removal of the core sample; (B) the sample core was very solid, and required fracturing it in multiple locations to remove it from the chimney; (C) sample material in the nose cone was left in place given the difficulty in removing it intact.

Regardless of the unexpected material behavior, the test embedded into the hardest material yet sampled by the system, at the highest impact velocity achieved, and demonstrated the potential for penetrators employed for sample return missions. The hybrid design of the steel tip prevented the flow stagnation seen in early evolutions, allowing the sample material to reach the SRC. The energy absorbing material along the length of the constant, 4 inch diameter of the penetrator was removed with the adjacent section of carbon fiber feed chimney, revealing the collected core sample (Figure 50). The exterior of the core exhibited a smooth surface that initially resembled clay, raising concerns that the system had filled prior to the collection of sandstone; however, this concern was unjustified given the minimal amount of soil overlying the rock, and once the core was removed from the feed chimney it was confirmed to be sandstone (Figure 51).

8.5. Phase II : 3rd Field Testing at Ione, CA, December, 2015.

Up to this point we hand not spent much time on the design of the sample return canister because much of the skepticism that we had received was on the survivability of the impact at 600 m/s. The above results showed that survivability was indeed possible, but the sample feed tube and canister needed a more careful design to as to survive the interior flow of mobilized rock material. This redesigned occurred over the summer of 2015 and included (a) Al collars for the nose cone section that matched the size of the rocket diameter, (b) Al feed tube (as opposed to carbon fiber) and (c) usage of a steel SRC instead of a thin Al SRC. The boost stage was also modified to take a single M6400 motor which would give a more consistent launch that using the four clustered K1440 that we used in the 2nd Field test. Using these motors eliminates the risk of non-simultaneous lighting of the motors but adds the risk that these single high thrust motors can on occasion be subject to failure of the forward enclosure.

With this redesign, a 3rd series of field test series were performed in Dec., 2015 at Ione, CA. The launch and impact of Gravedigger 5 is shown in Figure 52. The upward flight leg was very similar to that of the successful launches in the previous campaign and separation of the booster occurred soon after apogee. The downward leg was not perfect in that only 4 of the 8 outboard motors light resulting in an impact speed of about Mach 1 (~300 m/s). While less than desired, this speed is still in the desire operating regime. On impact the smoke grains which are used to track the rocket ignited producing a small smoke cloud above the impact sight.

The inspection of the impact sight shows similar cratering pattern with a small disturbed area about 0.3-0.6 m from the center of the impact. One difference though is the bulk of the outboard motors are intact, due to the reduced impact speed. Most importantly, the SRC is seen to have been ejected about 2 m from the center of the impact. It is fully intact

Figure 52. (a) Launch of the 3rd generation penetrator, (b) separation of booster and penetrator shortly after apogee (c) the penetrator at Mach 1 just above tree height, (d) impact and (e) close-up of the impact site showing the SRC ejected about 2 m from the impact sight.

On opening up the SRC (Figure 53) we find that a core sample has been successfully attained that retains the stratigraphy of the rock layers that were sampled by the penetrator prior to the ejection of the SRC. Closest to the top is top solid, followed by loose gravel. At the bottom is talc/sandstone. There are a few voids within the container which are believe to be from trapped air. These voids would not be present during space applications, and additional the sample is expected to be more compressed. In addition, we managed to have the SRC self-seal through beveling of the edges of the SRC which then fold under the force of the impact.

This is a crucial achievement for the project. When we started there was significant skepticism about the survivability of impacts at the proposed speeds, let alone the ability to eject the SRC through the debris of the impact. Through the above modeling and field testing, we have demonstrated that these key components to the concept of survivability and ejection are in fact very achievable.

There are two remaining issues – the ability to retrieve the ejected sample and what type of modifications to the material occur from the high velocity impact. These issues are addressed in the remaining two sections.

Figure 53. (a) Sample return canister after recovery, (b) the end of the canister showing partial self-sealing of the sample and (c) cutaway of the canister showing the captured sample including its stratigraphy.

9. Recovery Systems –Tethers and Other Options.

9.1. Tether Forces

In order to ensure that the tether does not snap the tether from the tension wave due to the pickup of a sample that has a high velocity relative, we must ensure two things: (i) the tether has sufficient strength to support the tension excursion, and (ii) the speed of sound in the tether material must be larger than the initial velocity discrepancy so that the tension can propagate without forming a shock wave in the material. The speed of sound in a solid rod is given by

$$c = \sqrt{\frac{Y}{\rho}} \tag{7}$$

where Y is the material's Young's modulus and ρ is its density. The candidate tether material Ultra-High Molecular Weight Polyethylene (UHMWP, branded as Spectra or Dyneema) has a

density of 970 kg/m^3 and a Young's modulus of 170 GPa, so the speed of sound in this material is in excess of 13 km/s. Consequently, shock wave damage to the tether is likely not to be a significant concern for sample pickup from small planetoids. Nonetheless, the tether will need sufficient strength to support any large tension excursion due to the large velocity discrepancy between the system and the sample on the surface.

In order to evaluate the peak loads and dynamics experienced by the tether in detail for the SaRSEE concept, we simulated the tethered sampling maneuver using our TetherSim software code, which integrates orbital dynamics propagators with tether cable dynamics models as well as models for other relevant physics. Using the output of our first-order optimization software to develop initial conditions of the tether deployment the retrieval of a 1 kg sample from the surface of Ceres was simulated. The scenario considered is shown in Figure 54. a 10-km long tether was used to retrieve a sample from a highly elliptical orbit with a periapsis altitude 10 km above the surface of Ceres, with an orbital velocity of 391 m/s. A 10-kg sampling penetrator was positioned at the end of the tether, with the tether deployed to a length of 7.5 km and set into rotation with an angular rate of 0.0524 rad/s. At the descending crossing of the orbital plane the tether was deployed at a rate of 110 m/s until the sampler contacts the surface. The sampler reached a peak velocity of 263 m/s before impacting the surface.

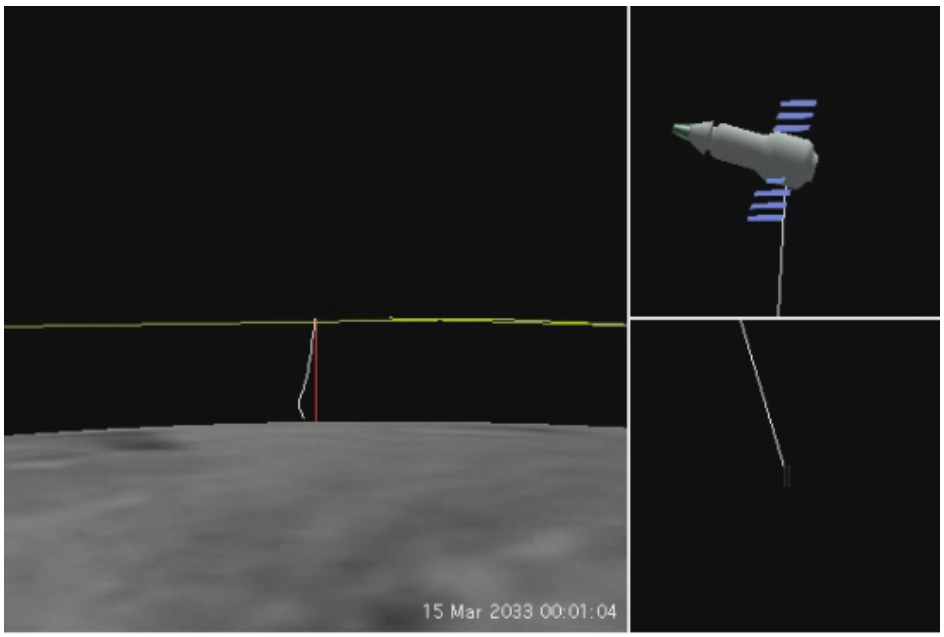

Figure 54. TetherSim model of penetrator deployment and recovery from the surface of Ceres. (Yellow shows the orbital path of the tether system, red shows the radius from the tether center of mass to the center of Ceres).

The TetherSim simulation results for this scenario are shown in Figure 55. The peak tension in the tether prior to impact is about 300 N. Impact occurs at t = 32 sec at which time tether deployment was halted. It is assumed that the impact of the sampler results in the sample canister being ejected upwards at a velocity of 60 m/s. The rotating tether then lifts the 1-kg

sample off the surface. Peak tether tension of 800 Newtons was observed after the deployment due oscillations included by the sample ejection. To sustain this tension excursion with a safety factor of 2, would require a braid composed of 13 yarns of 88 TEX Dyneema SK-75 yarn with a total mass of 11.4 kg, which is only 1.14X the sampling penetrator mass.

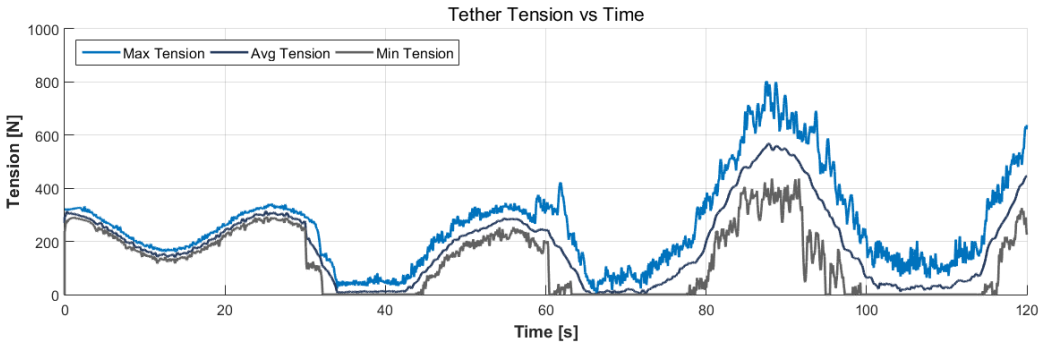

Figure 54. TetherSim Results for Elliptical Orbit Sampli

9.2. Tether Spin-Up Maneuver

The SRSEE concept calls for positioning the sampling mechanism at the end of a long tether, setting that tether into rotation, and using the tether's rotation to cancel some or all of the relative velocity between the host spacecraft and the target planetary body. There are several potential approaches for accomplishing spin-up of the tethered system, each with their own advantages and drawbacks.

Host Vehicle Thruster Spin-Up: The most straightforward method for spinning-up the tether system would be to deploy the tether and then fire the primary spacecraft's thrusters in a direction perpendicular to the tether and the desired spin axis. Low thrust over a long duration would be the preferred method to minimize development of tether oscillations. As long as the spacecraft needs to perform a ΔV maneuver equal to or greater than the desired tether tip velocity in order to place the spacecraft in the desired trajectory relative to the target body. This method will provide the simplest and lowest-mass-impact means of spinning up the tether. If the spacecraft uses a very low-thrust propulsion system, such as a Hall or ion thruster, the ΔV thrusting would ideally be modulated to facilitate the spin-up of the tether while maintaining the average thrust in the direction desired for rendezvous with the target object.

If, however, the spacecraft does not already need to perform a ΔV maneuver prior to passing the target object, or if the rendezvous ΔV direction is not well aligned with the desired spin plane, using host vehicle thrust will not be a mass-efficient method for spin up. Because the mass of the host vehicle will be much greater than the mass of the tether and sampler payload, the system's center of mass will be close to the host vehicle, and as a result thrust provided by the host spacecraft will have only a very short lever arm to generate the torque necessary to spin up the tether system. Consequently, the host will need to provide a total impulse sufficient to accelerate its entire mass by the desired tip velocity, and this will result in reducing the 'effective

Isp' for accelerating the sampler and tether by a factor roughly equal to the ratio between the sampler mass and the host spacecraft mass.

Sampler-Mounted Thruster Spin-Up: A more mass-efficient method for spinning up the tether system will be to use thrusters on the tether tip vehicle to provide the necessary thrust. Because this thrust at the tether tip will act over a much longer lever arm, it will generate the necessary torque with much lower propellant mass consumption. Again, a low-thrust, high-Isp propulsion solution acting over a long duration is preferable to minimize tether dynamical behavior and minimize mass requirements. In this case, the tether will provide a means to enable high-Isp electric propulsion to provide the ΔV necessary for the sample delivery and retrieval during a flyby, which would normally require high-thrust/low-Isp propulsion and thus significantly more propellant mass. However, performing EP thrusting at the tether tip will require additional mass for the power supply, electronics, and thruster components, increasing the tether tip mass. It is also unlikely that these components would survive the energetic impact with the planetoid surface, so they would be expendables.

Electrostatic Spin-Up: An alternate method for inducing the desired spin in the tether would be to coat the outside of the tether with a thin conducting layer and then charge the tether to high voltages so as to induce electrostatic drag forces through interaction with the solar wind, as in the 'electrostatic sail' concept originated by Pekka Janhunen of the Finnish Meteorological Institute To achieve the desired rotation velocity and spin vector, the tether would first be deployed in a direction perpendicular to both the desired spin axis and the solar wind velocity vector, and the high voltage bias applied to the tether would be modulated in phase with the rotation period to achieve net torque on the tethered system.

10. New Base-Line Concept

We have established that the SaRSEE sample return architecture is both feasible and has the potential to provide significant post-launch ΔV savings over state of the art mission concepts by leveraging flyby trajectories and hard impact sampling methods. However, in order to justify the development of the SaRSEE sampling and sample retrieval technologies they must provide a substantive, capabilities enhancing benefit to the sample retrieval mission beyond merely serving as suitable replacements for existing technologies. Through analysis of the sampling and sample retrieval mission phases we demonstrate that using a tether to both deliver the sampling penetrator to the surface and retrieve the extracted sample offers significant mass savings over the use of existing propulsion technologies, simplifies the mission architecture, and reduces risk of recovery failure.

While hard impact sampling represents significant technology development over state of the art sample acquisition technologies a key aspect of the hard impact sampling concept, the delivery of a high velocity penetrator to a small body, has already been demonstrated with existing technologies. In 2005 the Deep Impact mission successfully impacted the comet Tempel 1 at 10 km/s with a 370kg active impactor spacecraft [Mastrodemos et al., 2005]. While the Deep Impact mission did not recover a sample from Tempel 1, analysis of a hard impact sample mission to Ceres using a similar architecture and technology profile provides a representative baseline of the cost of such a mission utilizing sate of the art technologies against which the SaRSEE mission concepts we've developed can be compared.

As with the SaRSEE mission concepts already detailed, our baseline state of the art mission architecture utilizes hard impact sampling and a flyby of the target body to provide significant post launch ΔV savings over traditional sample return concepts. The flyby mission trajectory chosen as a starting point for our analysis was selected from a review of potential main belt asteroid sample return missions and includes 2 pre-encounter Mars flybys and 2 post-encounter Mars flybys and requires a post launch ΔV of approximately 1.6 km/s. The Ceres flyby itself is conducted at a relative velocity of 2.28 km/s which provides an impact velocity more than adequate for sample acquisition [Dankanich et al., 2010].

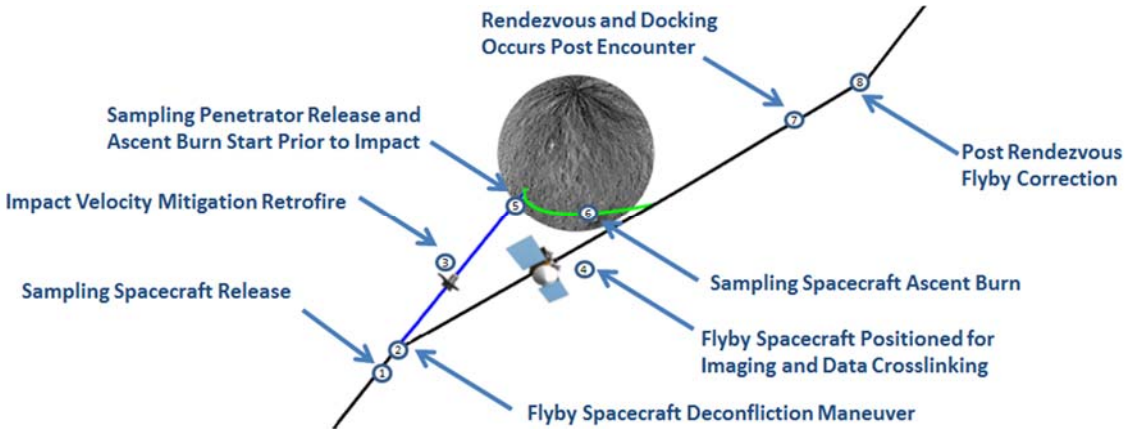

Figure 55. State of the Art Hard Impact Baseline Mission Ceres Encounter Profile.

Our baseline state of the art mission architecture, shown in Figure 55, utilizes three principle pieces of hardware: a primary flyby spacecraft, a sampling spacecraft, and a sampling penetrator. The flyby spacecraft is the primary spacecraft of the mission and hosts the sampling spacecraft which contains the sampling penetrator during cruise to the target body and carries the sampling spacecraft back to earth after the sample has been retrieved. The sampling spacecraft is a small but capable spacecraft that contains onboard power, communications, processing, imaging, and propulsion which is used to provide final guidance of the sampling penetrator to the target and return the sample to the flyby spacecraft once collected. The sample penetrator is as previously described, a penetrating sampler which allows for the collection of samples using hypervelocity impacts.

Figure provides a graphical overview of the baseline architecture encounter sequence; note that the high relative speed of the flyby spacecraft and sampling spacecraft result in nearly straight line trajectories. As with the Deep Impact mission design the flyby spacecraft arrives on trajectory which intercepts the target body. Prior to encounter with the target body the sampling spacecraft is released and the flyby spacecraft performs a deconfliction and delay maneuver. The timing of this maneuver is notionally selected for this analysis but during a mission would likely be chosen to provide adequate time and conditions for imaging of the sampling event. The size of the deconfliction maneuver is based on the updated aim point for the flyby, in this analysis chosen to optimize the ascent of the returned sample. Prior to impact of the sampling penetrator

an onboard propulsion system is used to perform at least one retrofire maneuver which is sized such that the penetrator impacts with an acceptable velocity (300 m/s - 600 m/s) and with an acceptable impact angle (within 5 of vertical). Small terminal guidance corrections maneuvers would be performed by an onboard RCS system utilizing either onboard or cross linked imaging to ensure the impact profile satisfies, velocity, angle, and target location and illumination constraints. Just prior to impact the sampling spacecraft releases the sampling penetrator on a short tether and begins its accent burn, resulting in a near zero relative velocity between the penetrator and sampling spacecraft at the time of impact. The sample is ejected from the sampling penetrator by the force of the impact and is retrieved by the sampling spacecraft via a short tether. The ascent burn continues until the sampling spacecraft is on the same trajectory as the flyby spacecraft. Rendezvous and docking of the sampling spacecraft with the flyby spacecraft is performed at some time after periapsis passage, and the pair returns to Earth after complementing two flybys of Mars.

Table 3. Baseline Encounter Profile Maneuver Requirements.

Spacecraft	Maneuver	ΔV [m/s]	Fuel Mass [kg]
Flyby Spacecraft	Deconfliction / Delay	225.9	44.0
Sampling Spacecraft	Retrofire	1,914.1	154.2
Sampling Spacecraft	Ascent Burn	4,233.8	117.6
Sampling Spacecraft	Rendezvous / Docking	242.1	2.8
Flyby Spacecraft	Post Rendezvous Flyby Correction	226.7	42.6

Table details the fuel requirements to complete a hard impact sample return mission utilizing state of the art technologies. The case in Table 3 assumes the high flyby speed of 2.2 km and smaller fuel requirements are needed if the ΔV of the flyby spacecraft is smaller. In order to generate the ΔV requirements for each segment of the mission profile the complete encounter sequence was optimized within a simulated in a MATLAB environment using custom orbit propagators and thruster models. The initial and post rendezvous flyby trajectories were provided as a boundary conditions of the optimization problem and designed based on the expected hyperbolic excess velocity at Ceres encounter and the desired impact angle of the sampling penetrator. The deconfliction maneuver needed to provide correct positioning of the flyby spacecraft during impact and match the departure trajectory of the sampling spacecraft was determined by the use of a single shooting optimization of the flyby spacecraft trajectory subject to constraints provided by the optimized ascent trajectory. The velocity mitigation retrofire conducted by the sampling spacecraft was sized in order to ensure the correct impact velocity and orientation of the sampling penetrator. Multiple shooting optimization of a sampling spacecraft ascent and departure trajectory was conducted to minimize the ΔV required to rendezvous with the flyby spacecraft. This ascent trajectory optimization was constrained to ensure that the sampling spacecraft would not impact the target, that a rendezvous could be made in a reasonable amount of time (< 24 hours), and that flyby trajectory provided sufficient clearance for the flyby spacecraft (> 10 km). The ΔV required of the sampling spacecraft to

rendezvous with the flyby spacecraft was determined based on the expected closure velocity of the spacecraft at rendezvous with a 2.0 factor of safety provided for docking operations. Finally the post rendezvous flyby correction was determined based on a maneuver needed to meet the outbound boundary conditions of the encounter. As demonstrated by our cursory analysis, recovering a hard impact sampler using state of the art propulsion would require several km/s of ΔV. While most of the ΔV required is needed by the sampling spacecraft, which due to its limited functionality and short operating lifetime can be made as small as possible thereby limiting the required fuel, the mission architecture would still require significantly more post launch ΔV then has ever been demonstrated by an interplanetary spacecraft.

Table 4. Mass Budget for Baseline Mission Architecture

Mission Component	Mass [kg]
Flyby Spacecraft	300
Sampling Spacecraft	25
Sampling Penetrator	10
Fuel	761.2
Total Mass:	**1096.2**

The ΔV requirements calculated for our baseline encounter profile combined with assumed properties of the sampling and flyby spacecraft can be used to determine a mass budget for the full mission concept, detailed in Table . In order to determine the fuel mass required in order to fly the profile shown in Figure some assumptions must be made about the spacecraft involved and the propulsion systems used. We assumed the sampling spacecraft was capable small spacecraft of 25 kg dry mass carrying a 10 kg sampling penetrator capable of collecting a 2 kg sample. Referencing previous interplanetary spacecraft designed with capabilities similar to those required for this mission, the flyby spacecraft was baselined as a 300 kg dry mass spacecraft utilizing bi-propellant thrusters (I_{sp} 270 s) for impulsive maneuvers during the encounter. In the analysis of the sampling spacecraft mission profile the thrust provided by the propulsion system was left as an open variable in the optimization. As a result the optimizer determined the optimal thrust level of the propulsion system to be 287 N. There are a number of potential propulsion systems, namely solid rocket motors and bipropellant thrusters, capable of providing the required performance with high propellant fractions. Due to their ability to be restarted and throttled we have chosen to baseline a bipropellant thruster (I_{sp} 270 s) as the primary propulsion for the sampling spacecraft. Using the rocket equation a representative fuel mass can be calculated for each segment of the mission profile for both spacecraft, as shown in Table . Incorporating estimates for the propellant required to fly the optimized ballistic solution for a Ceres sample return mission we determine a launch wet mass for the system of approximately 1100 kg. With an Earth departure characteristic energy requirement of 14.4 km^2/s^2 this mission design falls well within the launch capabilities of standard interplanetary mission launch vehicles such as the Atlas V 431 [Wise et al., 2010].

11. Modification of the Sample During High Velocity Impact.

Hypervelocity impacts of speeds greater than about 2 km/s produce metamorphism of the rocket material [Winter, 2001]. The issue is whether the high velocity impacts at speeds between 300 and 800 km/s being consider here produce such metamorphism. The International Union of Geological Sciences Subcommission of Metamorphic Rocks defines metamorphism as "…a subsolidus process leading to changes in mineralogy and/or texture (for example grain size) and often in chemical composition in a rock. These changes are due to physical and/or chemical conditions in a rock. These changes are due to physical and/or chemical conditions that differ from those normally occurring at the surface of planets and in zones of cementation and diagenesis below the surface" [Witold et al, 2003].

Metamorphism can be classified under five major categories: Contact Metamorphism is the result of thermal effects from intruding magma into cooler rocks; Regional Metamorphism is similar to Contact Metamorphism except on scales that make distinguishing individual contacts difficult; Hydrothermal Metamorphism is the result of interactions between minerals and water; Fault-Zone Metamorphism results in high-stress deformation in areas that experience large shear stresses; Impact Metamorphism results from the collision of meteorites and asteroids, or may occur during the explosion of a bolide [Winter, 2001]. Of the five categories, Impact Metamorphism differs the most in the higher temperatures and pressures created, as well as in the much shorter time-scales in which the alterations occur. Figure 56 shows pressure and temperature plots for various metamorphic facies that occur in Earth's lithosphere, as well as pressures and temperatures that occur during impacts.

Physical metamorphism is likely to occur form the pressures that arise on impact, and an outstanding issues remains where chemical metamorphism is occurring and if so what is the extent of damage to the sample. The pressures produced by the impact can be estimated as follows. For a 600 m/s penetration stopping in 1.5 m and assuming a constant deceleration stops in about 5 ms with an average deceleration of experiences an average deceleration of about 1×10^5 m/s/s. For a 20 kg penetrator, the force generated is about $\sim 2 \times 10^6$ N with an energy release of ~ 3 MJ. At first contact when only the cutting edge of the penetrator is in contact with the surface, the area is proportional $2\pi\, rd$ where r is the radius and d is the thickness of the nose cone. In the prototypes to date $r \sim 8$ cm and $d \sim 2$ cm yielding an area of about 5×10^{-3} m^2 and pressures of about 0.5 -1 GPa at the edges of the feedports. Once the feed points are filled with material the overall pressure will drop to about 100-200 MPa. However, because of the short time scale involved, significant temperature increases are unlikely so that from Figure 56 even at the highest pressures we are unlikely to be operating in the regime where chemical metamorphism can occur.

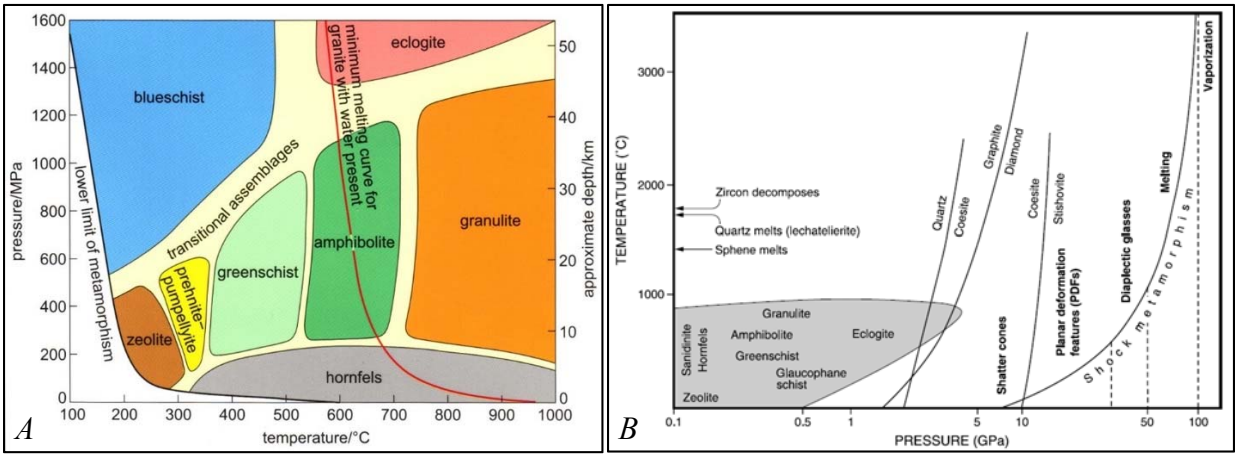

Figure 56. (A) Plot showing the metamorphic facies that occur at given pressures and temperatures, corresponding to the depths that these conditions exist at in the lithosphere, with pressure (in MPa) and depth shown on the vertical axis [Tindle, nd]; (B) plot showing temperatures and pressures generated during impact, with pressure (in GPa) shown on the horizontal axis, where the grey area corresponds to the temperature and pressure ranges shown in (A) [French, 1998].

Nevertheless the pressures are sufficiently large that physical metamorphism can occur, and this is seen in the core sample attained from Gravedigger 4. Figure 57 shows a close up of the cross section of the recovered core sample from Figure 50. Note that the surface of the sample has a smooth texture which is a modification of the rock produced by the impact. In addition the density of the sample appears to be higher than that of the reference sample taken from undisturbed material near the impact site. The measured density of the undisturbed material was measured as 1.66 gm/cm^3. The density of the sample core was measured at 2.13 gm/cm3. Thus, there is about a 25% increase in density due to the filling of voids in the rock from the compressive forces from the impact.

Figure 57. *Close of the sample shown in Figure 50 from Gravedigger 4. The ring in the cross-section indicates that this one area is modified by the high velocity impact.*

In addition to the change in texture of the material there is a red ring seen in the sample which is clearly due to the impact. We are still awaiting the chemical analysis of the sample but the present thought is that this ring is iron oxide. There are three potential sources of iron oxide:

(1) it originates from the steel tip which in the presence of ground moisture and high pressure oxides and is scraped off the tip as the sample moves up the feed tubes. The sample shows this red material along the surface of the sample which coincides with the side feed ports in the nose cone.

(2) It originates from reorganization of existing iron oxide in the sample. An image of the thin section under polarized light for the reference and core samples is shown in Figure 2.A crack in the reference sample is seen in the middle of Figure 2a. The red ring in the core sample is seen on the left hand side of Figure 2b, and has a very different appearance than the crack. The different minerals can be identified by color in the image. Quartz appears as the yellow crystals in the images and their appearance between the reference and core samples are essentially the same indicating that there is no damage from shocks produced by the impact. Iron oxide appears as red in the images and is present in both the reference sample and in the core. In the core sample this material appear to have been depleted to the left of the red line while still be in abundant to the right. The interpretation which is still under investigation is that this material was made more mobile during the impact which lasts only for a few ms. As the shock wave from the impact dissipates in the core sample this more mobile mineral precipitates to form the observed thin red line.

(3) The third interpretation is that there is chemical metamorphism occurring and that we may be underestimating the pressures and temperature that develop during the impact. We are stilling access to a microprobe to test this hypothesis.

If the latter is occurring then we may have to set a maximum speed limit for the impact velocity in order to avoid such alteration. If it coming from oxidation of the nose cone then this would be an artifact of terrestrial testing and would not occur if in space due to the lack of ground water. It

is arises from flow dynamics through the feed ports that it could be minimized by the design of the feed ports and/or reducing the speed of the impact.

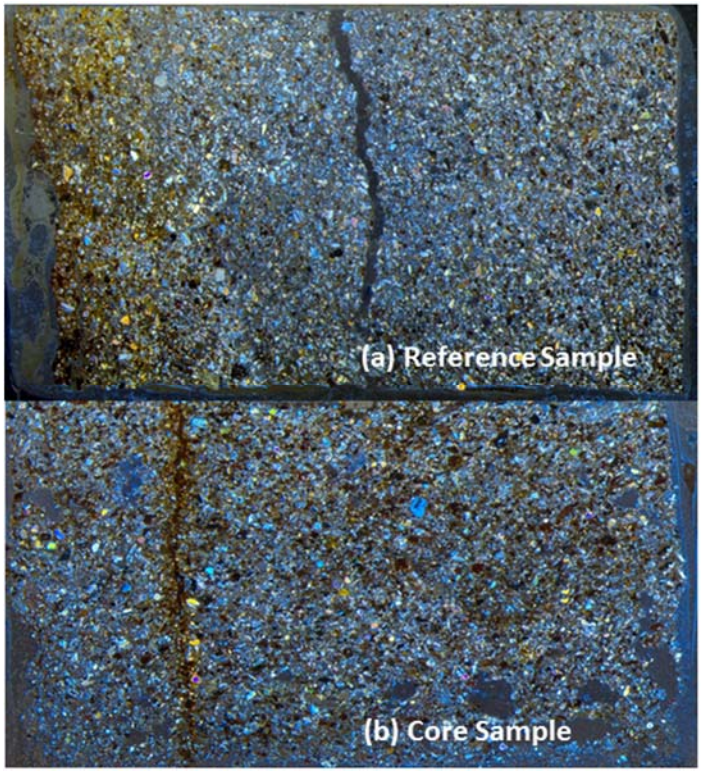

Figure 58. Images of thin sections of the reference and core samples under polarized light. Some different mobility of some of the mineral appear to occur to produce the red line in the sample but otherwise the material properties between the reference and core samples appears to be the same.

12. Conclusion.

The concept of sample return utilizing high velocity impactors started at the very lowest technology readiness level imaginable. Under the support from NIAC we have taken this concept and demonstrated not only survivability for impacts speeds up to 600 m/s (~ Mach 2) but demonstrated that a core sample can be attained and self-ejected. This core sample can retain the rock stratigraphy with possibly only a small modification to the inherent mineral structure. Recovery of the sample from attached tethers looks entirely feasible and that the mass budget could be accommodated by Discovery or New Frontier range of missions.

We are deeply indebted to NIAC for its support as we moved from concept to demonstration under relevant conditions. Our efforts show that sample return using high velocity impacts can greatly open up space exploration and lead to a greater understanding of the origins

of the solar system as well potentially being able to bring back to Earth significant samples from high value solar system objects with the mission requirements of present day systems.

13. References

Asphaug, E. 2009. "Growth and Evolution of Asteroids". The Annual Review of Earth and Planetary Sciences, 39:413-48. doi: 10.1146/annurev.earth.36.031207.1274214.

Brucato, J. R., A. Rotundi, E. Mazzota Epifani. 2009. "Sample Return Missions from Minor Bodies: Achievements, Future Plan and Observational Support". Earth Moon Planet, 105, 273-282. doi: 10.1007/s11038-009-9336-5.

Brunetto, R.. 2009. "Space Weathering of Small Solar System Bodies". Earth Moon Planet, 105:249-255. doi: 10.1007/s1038-009-9340-9.

Chapman, C.R.. 1996. "S-type asteroids, ordinary chondrites, and space weathering: The evidence from Galileo's fly-bys of Gaspra and Ida". Meteorites & Planetary Science 31, 699-725.

Dankanich, John W., et al. "Main Belt Asteroid Sample Return Mission Design." *AIAA* 7015 (2010): 25-28.

Drake, M.J., K. Righter. 2002. "Determining the composition of the Earth". Nature, Vol. 416, 39-44.

ESA. 2014. Image: Rosetta at Comet. ESA/ATG Medialab. http://www.esa.int/var/esa/storage/images/esa_multimedia/images/2014/11/rosetta_at_comet_landscape/15031338-1-eng-GB/Rosetta_at_Comet_landscape.jpg

French, B.M.. 1998. *Traces of Catastrophe: A Handbook of Shock-Metamorphic Effects in Terrestrial Meteorite Impact Structures.* LPI Contribution No. 954, Lunar and Planetary Institute, Houston. Page 32.

Institute of Space and Astronautical Science (ISAS). 2008. "LUNAR-A". Japan Aerospace Exploration Agency. http://www.isas.jaxa.jp/e/enterp/missions/lunar-a/.

JAXA. 2003. "Asteroid Explorer Hayabusa2". Satellites and Spacecraft. Japan Aerospace Exploration Agency. http://global.jaxa.jp/projects/sat/hayabusa2/index.html.

JPL Special Review Board. 2000. "Report on the Loss of the Mars Polar Lander and Seep Space 2 Missions". Jet Propulsion Laboratory, California Institute of Technology. JPL D-18709.

Janhunen, P., Electric sail for spacecraft propulsion, *J. Prop. Power*, 20, 763-764, 2004.

Lorenz, R.D.. 2011. “Planetary penetrators: Their origins, history and future”. Advances in Space Research, 48, 403-431. doi: 10.1016/j.asr.2011.03.033.

Lorenz, R.D., J.E. Moersch, J. A. Stone, A. R. Morgan Jr, S.E. Smrekar. 2000. “Penetration tests on the DS-2 Mars microprobes: penetration depth and impact velocity”. Planetary and Space Science 48, 419-436.

Malik, T. 2015. “It’s Alive! Comet Lander Philae Phones Home After Months of Silence”. Space.com. http://www.space.com/29661-philae-comet-lander-wakes-up.html

Marín, D.. 2014. “Manda tu nombre al asteroid Bennu”. Eureka, 18 Jan., 2014. Images credited to NASA. http://danielmarin.naukas.com/2014/01/18/manda-tu-nombre-al-asteroide-bennu.

Mastrodemos, Nikos, Daniel G. Kubitschek, and Stephen P. Synnott. "Autonomous navigation for the deep impact mission encounter with comet Tempel 1." *Space Science Reviews* 117.1-2 (2005): 95-121.

Meyer, A.. 2009. “Genesis Search for Origins: Mission History”. NASA, Jet Propulsion Laboratory, California Institute of Technology, Pasadena, CA. http://genesismission.jpl.nasa.gov/gm2/mission/history.htm.

Mizutani, H.. 1995. “Lunar Interior Exploration by Japanese Lunar Penetrator Mission, LUNAR-A”. Journal of Physics of the Earth, 43, 657-670.

Mueller, R.P., P.J. van Susante. 2012. “A Review of Extra-Terrestrial Mining Robot Concepts”. *Earth and Space 2012: Engineering, Science, Construction, and Operations in Challenging Environment, Symposium 2: Exploration and Utilization of Extraterrestrial Bodies*. ASCE. doi: 10.1061/9780784412190.034

Nakajima, T., M. Hinada, H. Mizutani, H. Saitoh, J. Kawaguchi, A. Fujimura. 1996. “LUNAR PENETRATOR PROGRAM: LUNAR-A”. Acta Astronautica, Vol. 39, No. 1-4, pp. 111-119.

NASA. nd. “OSIRIS-Rex Exploring Our Past, Securing Our Future Through Pioneering Asteroid Science”. Goddard Space Flight Center, Greenbelt, Md.. http://www.nasa.gov/centers/goddard/pdf/552572main_OSIRIS_REx_Factsheet.pdf

National Research Council. 2005. *Effects of Nuclear Earth-penetrator and Other Weapons*. The National Academies Press. Washington, D.C. Web. http://www.nap.edu/openbook.php?record_id=11282

National Research Council, Committee on the Planetary Science Decadal Survey. 2011. “Vision and Voyages for Planetary Science in the Decade 2013-2022”. National Academy of Sciences, Washington DC. www.nap.edu.

Neal, C. R.. 2009. “The Moon 35 years after Apollo: What’s left to learn?”. Chemie der Erde, 69, 3-43. doi:10.1016/j.chemr.2008.07.002

Neal-Jones, N., B. Steigerwald, R. Garner Ed. 2013. Image: OSIRIS-Rex, TAGSAM. NASA Goddard Space Flight Center, Greenbelt, Md..
http://www.nasa.gov/topics/solarsystem/features/osiris-rex-security.html

Sandford, S. 2014. “An Overview of the OSIRIS-REX Asteroid Sample Return Mission”. SSERVI Exploration Science Forum. NASA Ames Research Center, Bld. 152. Moffet Field, CA. 21 July 2014. Invited speaker.

Shevchenko, V.G., R.A. Mohamed. 2005. “Spacecraft Exploration of Asteroids”. Solar System Research, Vol. 39, No. 1, 2005, 73-81.

Surkov, Y.A., R.S. Kremnev. 1998. “Mars-96 mission: Mars exploration with the use of penetrators”. Planetary Space Science, Vol. 46, No. 11/12, pp.1689-1696.

Todd, N. S.. 2015. “Hayabusa Asteroid Itokawa Samples”. NASA, Curation, Hayabusa. http://curator.jsc.nasa.gov/hayabusa.

Tindle, Andy. nd. “Reference Cards for Geologists, Metamorphic Facies.”
http://www.open.ac.uk/earth-research/tindle/AGT/AGT_Home_2010/Ref_Cards.html.

Ulamec, S., J. Biele, P.W. Bousquet, P. Gaudon, K. Guerts, T.M. Ho, C. Krause, C. Lange, R. Willnecker, L. Witte. 2014. “Landing on small bodies: From the Rosetta Lander to MASCOT and beyond”. Acta Astronautica, 93(2014), 460-466. doi: 10.1016/j.actaastro.2013.02.007.

Whalen, A.. 2009. “Stardust NASA’s Comet Sample Return Mission”. NASA, Jet Propulsion Laboratory, California Institute of Technology, Pasadena, CA. http://stardust.jpl.nasa.gov/home/index.html.

Winglee, R. M., C. Truitt, R. Hoyt. 2013. “Sample Return Systems for Extreme Environments”. Final Report for NNX12AR02G. NASA.
http://www.nasa.gov/sites/default/files/files/Winglee_2012_PhI_SampleReturnExtreme.pdf.

Winter, J.D.. 2001. *An Introduction to Igneous and Metamorphic Petrology*. Upper Saddle River: Prentice-Hall, Inc.. Print.

Wise, M. A., J. M. Lafleur, and J. H. Saleh. "Regression Analysis of Launch Vehicle Payload Capability for Interplanetary Missions." *61st International Astronomical Congress*. 2010.

Witold, S., J. Desmons, D.J. Fettes, B. Harte, F.P. Sassi, R. Schmid. 2003. “A systematic nomenclature for metamorphic rocks: 2. Types, grade and facies of metamorphism.” *Recommendations by the IUGS Subcommission on the Systematics of Metamorphic Rocks.* Web version. http://www.bgs.ac.uk/scmr/docs/papers/paper_2.pdf.

Yano, H., T. Kubota, H. Miyamoto, T. Okada, D. Scheeres, Y. Takagi, K. Yoshida, M. Abe, S. Abe, O. Barnouin-Jha, A. Fujiwara, S. Hasegawa, t. Hashimoto, M. Ishiguro, M. Kato, J. Kawaguchi, T. Mukai, J. Saito, S. Sasaki, M. Yoshikawa. 2006. "Touchdown of the Hayabusa Spacecraft at the Muses Sea on Itokawa". *Science*, New Series, Vol. 312, No. 5778, pp. 1350-1353.

Yeomans, D.. 2005. "Hayabusa's Contributions Toward Understanding the Earth's Neighborhood". NASA, Jet Propulsion Laboratory, California Institute of Technology, Pasadena, CA. http://neo.jpl.nasa.gov/missions/hayabusa.html.